Summer 2013

Heterogeneous Finite Element Stress Analysis of Abdominal Aortic Aneurysms : Comparison Between Ruptured and Unruptured Lesions

Timothy Kwang-Joon Chung
University of Iowa

HETEROGENEOUS FINITE ELEMENT STRESS ANALYSIS OF ABDOMINAL AORTIC ANEURYSMS: COMPARISON BETWEEN RUPTURED AND UNRUPTURED LESIONS

by

Timothy Kwang-Joon Chung

A thesis submitted in partial fulfillment
of the requirements for the
Master of Science degree in Biomedical Engineering in the Graduate College
The University of Iowa

August 2013

Thesis Supervisor: Professor Madhavan L. Raghavan

Graduate College
The University of Iowa
Iowa City, Iowa

CERTIFICATE OF APPROVAL

MASTER'S THESIS

This is to certify that the Master's thesis of

Timothy Kwang-Joon Chung

has been approved by the Examining Committee
for the thesis requirement for the Master of Science Degree in Biomedical Engineering
at the August 2013 graduation.

Thesis Committee: _____
Madhavan L. Raghavan, Thesis Supervisor

_____
Joseph M. Reinhardt

_____
Nicole M. Grosland

_____
Edward Sander

_____
Sudershan K. Bhatia

To good old days

Calvin: 'I'm a genius, but I'm a misunderstood genius'
Hobbes: 'What's misunderstood about you?'
Calvin: 'Nobody thinks I'm a genius'

-Bill Watterson in Calvin and Hobbes

ACKNOWLEDGMENTS

I would like to take this opportunity to acknowledge those who have graced me with their presence. I am humbled and grateful to those who have given me a chance to flourish. I would like to think that I am not too old to realize that I am still a work in progress and that I will get there eventually, wherever there may be. I am thankful for all my friends that have stuck around through the many seasons of life and to the memorable moments and conversations. Rather than listing names, you should know who you all are. I have also had many mentors that have shared their wisdom (even if it seemed like I wasn't paying attention). Special thanks to Grace Shin, Jong Koo Lee and Tony Shebek for all of their wisdom.

I would like to take the time to thank the University of Iowa Biomedical Engineering department for their expertise in their respective fields and for keeping me interested in the field. Special thanks to my undergraduate advisor Professor Tae-Hong Lim for the encouragement and accountability. This body of work would not have been possible without my advisor, Professor M.L. Raghavan. There is still much to learn, but in the meantime thank you for the time, guidance and patience.

I would like to thank my family for all their love and support. I am grateful for my aunt and uncle June and Charles Yang for providing wonderful opportunities and memories (e.g. shoveling cow manure on your garden) and to Y.H and S.J Baek for all their support. To my cousins Jennifer, Lynn and Stacy for being more like sisters to me. A shout out to Professor George Thomas for showing me that programming isn't a necessary evil. To my brother for always trying to lead me in the right direction and to his family. To my cousins in Canada and Korea and my grandparents. I would like to dedicate this thesis to my parents. Although they

did not directly help me on this thesis, I am an extension of who they are. Thank you for your love, kindness and patience…so far.

Lastly, to those raccoons late at night running across the street and scaring me half to death as I drive, yes, you know who you are.

TABLE OF CONTENTS

LIST OF TABLES

LIST OF FIGURES

CHAPTER 1: INTRODUCTION

Abdominal aortic aneurysm (AAA) is a diseased condition of the artery that can be described as an irreversible ballooning of the aorta during the course of an individual's life. The aorta is major conduit for oxygenated blood flow out of the heart into the rest of the body and its peripheral limbs. The abdominal aorta refers to the aorta in the abdomen region that has blood flow outlets (renal arteries) to the kidneys and blood flow outlets (iliac arteries) to the lower trunk (Figure 1). For a normal healthy adult, the aorta will have a diameter of about 2 -2.5 centimeters (cm).

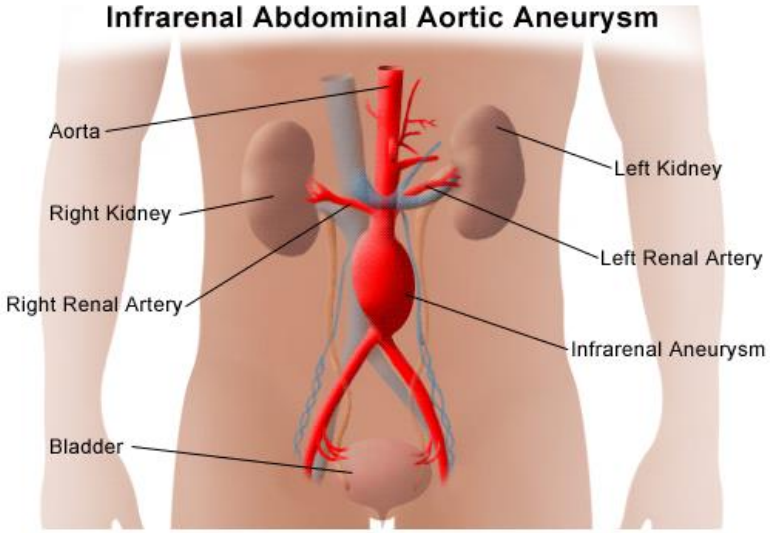

Figure 1*: Abdominal Aortic Aneurysm physiologic location with renal arteries flowing oxygenated blood to the left/right kidneys and the iliac arteries flowing blood to the left/right leg.*

For unknown reasons, the abdominal aorta undergoes internal injury that leads to subsequent remodeling of the artery wall and an undesirable dilation of the aorta under physiologic pressure and elevated pressure due to hypertension over millions of cardiac cycles.

Diseased aneurysms can reach up to diameters of 7 cm and usually exhibit asymmetric growth that cannot be easily predicted. Aneurysms are most prevalent in western societies among the elderly population. Still it remains the 13th leading cause of cardiovascular related deaths in the United States [5].

Although there are other complications that arise with having a dilated abdominal aorta, the major risk and concern is aneurysm rupture. Rupture of an aneurysm is a single catastrophic event that penetrates the artery wall completely and causes severe internal bleeding. Ruptured aneurysms will most likely result in death if there is no immediate intervention as the mortality rates are high due to complications from internal bleeding [6].

Aneurysms pose several clinical challenges in diagnoses and intervention. Physicians are able to detect aneurysms by feeling the abdomen region providing that the patient is not too overweight. However, aneurysms are often detected unexpectedly by computed tomography (CT scan) or through elective ultrasound screening. After the presence of an aneurysm is known, the next challenge is to determine what treatment, if any to undergo.

Table 1: Darling et al findings tabulated of a relatively large aneurysm population of rupture and diameter [1].

Size (cm)	Ruptured	Unruptured	Total	%Ruptured
≤ 5.0	34	231	265	12.8
> 5.0	78	116	194	40.0
No size recorded	6	8	14	43.0
Total	118	355	473	24.9

It has been a long held ‘rule of thumb’ or criteria that aneurysms with a maximum diameter greater than 5 to 5.5 centimeters (cm) should have surgical intervention. In 1977 Darling et al. reported that there were still many aneurysms less than 5 cm that were rupturing [1]. Darling et al. reported that 12.8% of aneurysms with a diameter less than or equal to 5 cm ruptured (34 ruptured out of a 265 total aneurysms), while 40% of aneurysms with a diameter greater than 5 cm ruptured (78 ruptured aneurysms out of 194 total aneurysms) and a rupture occurrence of 24.9% of all aneurysms ruptured (Table 1). This has been a preface for much speculation in the course of AAA rupture research as it cannot be simply stated that larger diameter aneurysms will rupture while smaller diameter aneurysms will not rupture.

Aneurysm rupture is a catastrophic event that has a high morbidity rate. There has been much interest in the medical and biomedical engineering communities to understand the mechanics of rupture. Studies investigating material properties of the diseased aneurysm wall, material components of the artery wall, experimental testing to see the maximum mechanical stresses of diseased wall tissue and computational methods have aided in the process of understanding the mechanics of rupture [4, 5, 7-23].

Arterial Wall and its Properties

The arterial system is a living conduit that is able to undergo repair and remodeling within the body. In the diseased state of an aneurysm, it was found that the elastin, smooth muscle content decreased while the collagen and ground substance content increased [24]. The artery wall is composed of countless molecules that are organized into fibers that make up the wall tissue. The major fiber components that help retain the shape of the artery are elastin and

collagen. The biochemical aspects of these fibers will not be discussed, but rather their mechanical contributions to the wall.

Elastin bands in the wall tissue are elastic components of the tissue. Elasticity is the ability for a deformed shape under a load to retain its original configuration when the load is withdrawn. As the wall tissue continues to deform, the elastin fibers become taut and collagen fibers are recruited. Collagen fibers are able to withstand a much higher load than the elastin fibers, but they are unable to retain the original undeformed state.

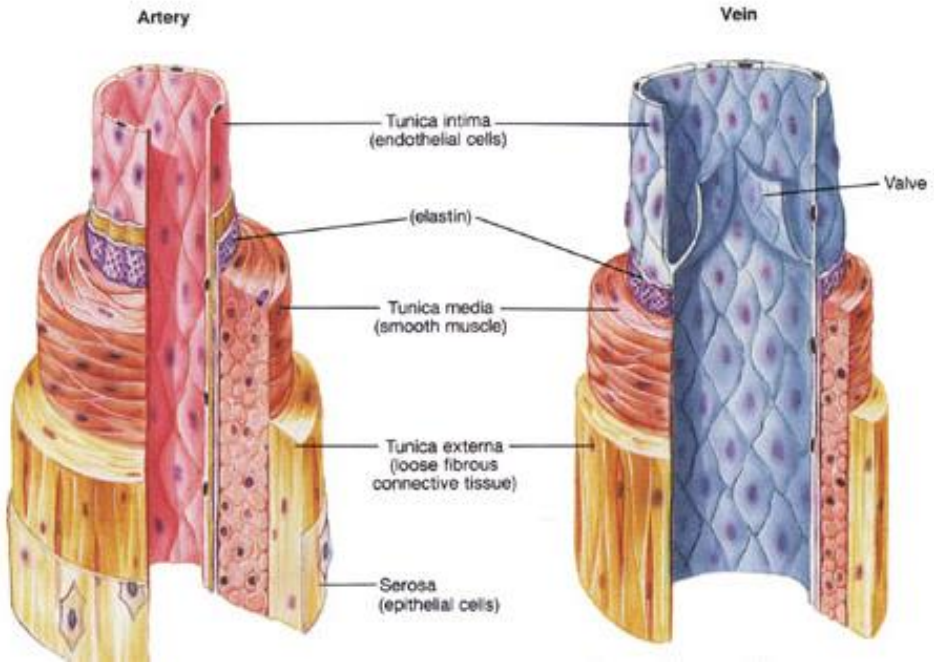

Figure 2: *The layers of the arterial wall are shown beginning with the inner layer of endothelial cells (intima layer), smooth muscle (media), connective tissue (externa) and outermost layer known as the serosa .*

The greatest heterogeneity of the wall tissue occurs across the thickness of the wall. The components of the wall are fused together but are given assigned layers as convention. The inner layer where blood flows is known as the intima layer, the media is the middle layer

composed of smooth muscle cells, elastin and collagen, and the adventitia is the outermost layer that is composed of collagen and elastin (Figure 2). For all practical purposes, the mechanical contribution of these 'layers' are relatively undefined. The effect of this heterogeneity was relatively unknown until Humphrey et al. first reported the concept of residual stresses of an artery (across the thickness). Humphrey et al. found that the residual stresses across the artery wall thickness helped homogenize the circumferential stress [25].

Uniaxial extension tests have been performed on artery wall tissue that characterizes the indiscriminate contributions of the entire wall and the maximum load the artery wall can accept across longitudinally or circumferentially. These characterizations only describe the bulk stresses the entire wall can withstand and not what the wall can accept through its heterogeneous wall thickness (where actual rupture occurs). The nonlinearity of aneurysm wall tissue under load has been extensively reported on by Raghavan et al. and others [4, 16, 18, 20, 26] and many material models have been formulated from experimental data.

Figure 3 represents a sample uniaxial extension test, where the 'toe region' represents the wavy elastin fibers becoming taut, while the higher stress/strain region represent the recruitment of collagen fibers. Equation 1a – 1b refers to how stress is calculated incorporating the changes in the mid cross sectional area as the tissue continues to stretch with the assumption of the material being isotropic with no volumetric changes as the material is being stretched.

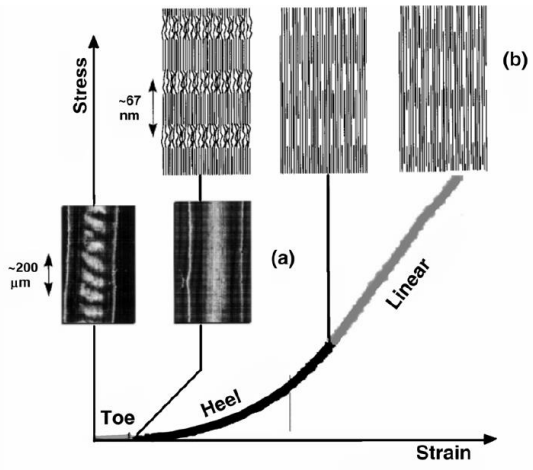

Figure 3: Elastin recruitment (toe region), combined stretching in the heel region, and the linear region of mostly collagen fibers. [27]

The peak stress of the artery sample represents the stress across the entire thickness of the wall. Equation 1a encompasses the maximum stress with the actual cross-sectional area (stress along the thickness), and Equation 1b refers to the maximum tension with the thickness lumped together [16]. Failure stress normalizes the thickness contributions and reports the cross sectional area change with an assumption of material isotropy.

$$Equation\ 1a:\ \ S_f = \frac{F_f}{w_o t_o}\left(1 + \varepsilon_f\right)$$

$$Equation\ 1b: T_f = \frac{F_f}{w_o}\left(\sqrt{1 + \ \varepsilon_f}\right)$$

$$S_f = Failure\ Stress;\ T_f = Failure\ Tension;\ \epsilon_f = Failure\ Strain;$$

$$w_o = Original\ width; t_o = \ Original\ Thickness$$

Failure tension eliminates the uncontrollable characteristics of thickness and describes the propensity of the wall to fail along its entire thickness. The contribution of thickness is ignored when using tension and may help clarify the 'maximum' load the arterial wall may withstand in a purely geometric sense. Therefore, tension will be considered as the index of interest for comparisons of ruptured and unruptured aneurysms with stress being presented as a formality to what has been traditionally reported in literature.

Computational Models and Material Definitions

Computational finite element models have been used to help describe the behavior of an aneurysm under idealized physiologic conditions (pressure induced to systolic pressure). For any predefined AAA surface geometry, there are several required parameters that describe the aneurysm material properties. A wide range of material models have been used in the past to describe how the material deforms under a certain loading condition. Simple model assumptions using linear Young's Elastic modulus and Poisson's Ratio from traditional mechanics were used to describe earlier AAA computational models.

In the early stages of soft tissue experimentation, researchers used simple mathematical models to mimic the nonlinear behavior in uniaxial testing [28]. Many of the material mathematical models were developed before finite element computational modeling became readily available. The mathematical material models were derived from experimental methods. Rivlin et al. proposed a neo-Hookean material model describing the non-linear behavior of the stress-strain curve and another model known as the Mooney-Rivlin hyperelastic material was developed. Fung et al. developed an exponential strain energy function that described the general behavior of soft tissues [29] that led to the innovation and descriptions of material models that were specific to a certain type of soft tissue.

Raghavan and Vorp [18] described a material model for aortic aneurysmal tissue using measured data from extension tests, and presented a new hyperelastic material model found in Equation 2 [18]. A Material model proposed by Raghavan and Vorp is a strain energy density function for a homogenous, incompressible, isotropic and hyperelastic material [18]. The material model is assigned two coefficients (α, β) that describes the load-deformation curve (R^2 = 0.96, fit to experimental data). In the same study, a computational finite element model was constructed using a single averaged alpha and beta coefficient from experimental data.

Equation 2: *Strain energy function describing the arterial wall.*

$$W = \alpha(I_B - 3) + \beta(I_B - 3)^2,$$

$$I_b = Trace\ B\ (Cauchy - Green\ Tensor), \alpha\ \beta\ material\ Parameter$$

Maier et al reported the effects of material model assumptions on finite element models in 2010 [20]. This study covered simple material assumptions with linear geometry, simple material assumptions with nonlinear geometry, and a nonlinear hyperelastic material model [18] describing the entire AAA. All models had assumed uniform thickness and uniform material properties. Maier et al scheme of material models for uniform thicknesses will be used in the current study as well in addition to variable wall parameters (variable thicknesses and variable material properties).

Post-Mortem Aneurysm Research

Thubrikar et al. completed a study on the mechanical properties of aneurysms in different regions of the aneurysm [21]. The research group excised five whole aneurysms with diameters greater than 5 cm. It was found that the posterior regions were thicker than the anterior regions and that the wall stiffness increased from the posterior to anterior to lateral regions of the aneurysm. A total of 46 longitudinal and circumferential strips were tested with a total of 47 thickness measurements. The purpose of the study was not to test a hypothesis but rather report qualitatively and quantitatively the characteristics of diseased aneurysms.

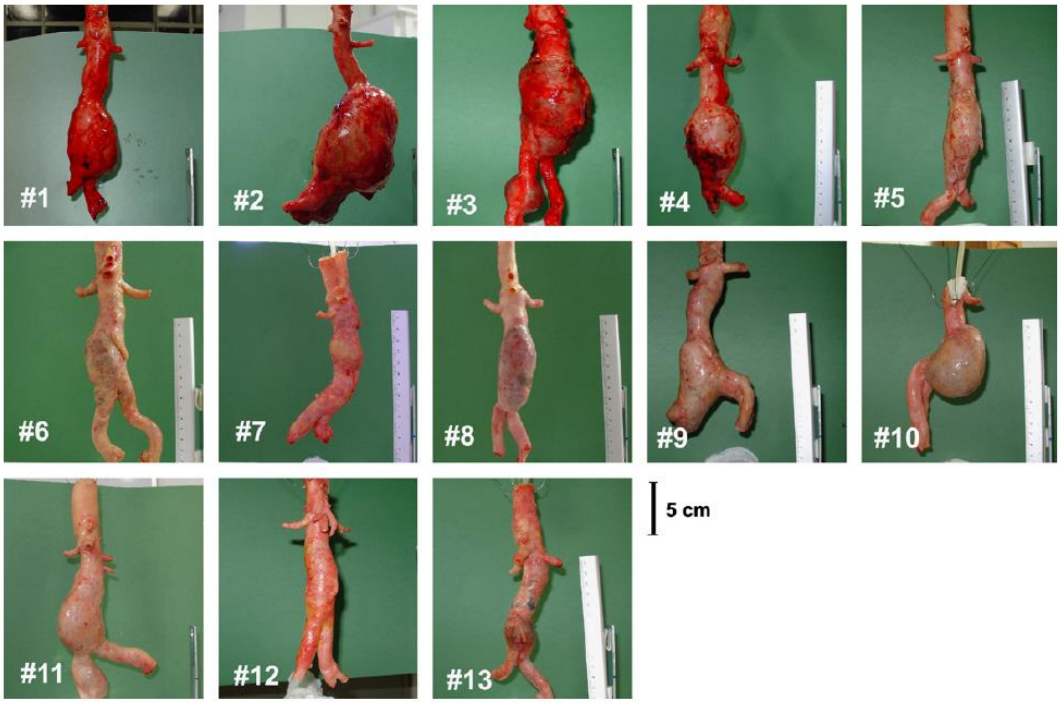

Figure 4: Aneurysms 1-4 ruptured and Aneurysms 5-13 unruptured [4].

Raghavan et al. completed a study that was similar in nature to Thubrikar's work with a greater density of measurement [4]. They retrieved measured data from post-mortem patients with diseased aneurysmal tissue. A total of thirteen aneurysms were excised that included

four ruptured aneurysms and nine unruptured aneurysms (Figure 4). All aneurysms were examined and tested with the same protocol within 48 hours of autopsy [4]. Wall thicknesses were measured with a digital caliper in the anterior, posterior, right and left regions of the aneurysm with about 40 measurements per aneurysm. Uniaxial extension tests were performed on about 6 specimens per aneurysm with consistent geometry (aside from thickness) per aneurysm and force displacement data was collected for analysis. Specimens were taken in the longitudinally oriented direction with a few specimens taken in the circumferentially oriented direction. Histology was performed on a strip adjacent to the uniaxial extension test specimens as well. In addition to the measured data collected, 36 digital photographs revolving around the aneurysm were taken in front of a green background for each aneurysm of interest.

Failure properties (strength, tension), wall thicknesses, zero-pressure geometry, and histological data are information that cannot be retrieved without excising the entire aneurysm. Martufi et al. used the radius of curvature to predict the aneurysm wall thickness and Vande Geest et al. proposed a stochastic model that predicted failure strength of the aneurysm in order to calculate the Rupture Potential Index (RPI) of an aneurysm (Equation 7) [13, 23]. The study completed acquired direct wall thickness measurements as well as failure properties of the aneurysms [4, 16].

The thirteen aneurysms were labeled numerically from 1 – 13, with 1-4 being the ruptured aneurysms. Table 2 (adapted from [4]) corresponds to all of the aneurysms seen in Figure 5 and gives basic background information of each aneurysm.

Table 2: Aneurysm ID with age, aneurysm status, aneurysm diameter, number of material strips and thickness sites collected in [4].

ID	Age	Rupture Status	Diameter (cm)	Strips	Thickness Sites
1	66	Ruptured	5.06	5	33
2	75	Ruptured	7.93	6	36
3	70	Ruptured	6.83	5	46
4	69	Ruptured	5.48	5	26
5	74	Unruptured	4.06	6	28
6	79	Unruptured	3.84	8	26
7	84	Unruptured	3.2	4	43
8	46	Unruptured	3.35	4	20
9	69	Unruptured	4.31	10	28
10	80	Unruptured	6.58	2	20
11	84	Unruptured	4.46	11	37
12	79	Unruptured	3.31	6	28
13	90	Unruptured	3.57	5	48

Raghavan et al. tested the hypothesis of whether or not ruptured aneurysms were weaker than unruptured aneurysms [4]. It was found that ruptured aneurysms were not weaker (on average) than unruptured aneurysms for the given study population. Figure 5 represents the aneurysm diameter and failure tension. Regardless of ruptured or unruptured status and diameter, the failure properties of the aneurysms were found to be statistically insignificant as the ruptured aneurysms were found to be within the range of the minimum failure tension of the unruptured aneurysms.

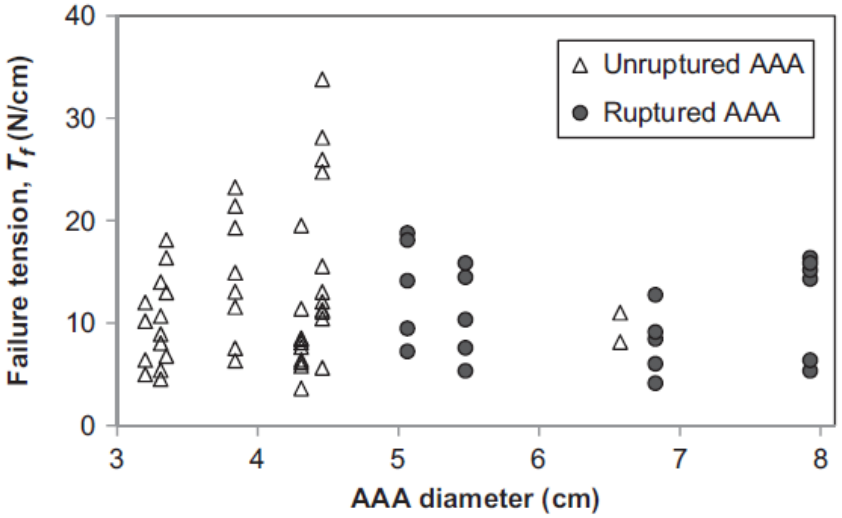

Figure 5: Failure tension properties of each aneurysm. Aneurysm diameter (cm) and Failure Tension (N/cm) of all Abdominal Aortic Aneurysms in the data set.

Study Objective

Why do some aneurysms rupture while others do not? Raghavan et al. reported that ruptured aneurysm tissue was not weaker on average than unruptured wall tissue [4]. A simplistic way of viewing the problem is to ask the question *is rupture caused by nature or nurture?* It may be that the aorta wall has deteriorated over time (nature) or that the aneurysm was subject to an abnormally high physiologic pressure (nurture). Rupture could be described as a combination of the two events (abnormal tension elevation or abnormal failure tension drop), but one may have a greater influence in why aneurysms rupture when they do.

The previous study performed by Raghavan et al. reported the effects of the wall material properties and diameter over time, there is no evidence that rupture occurs because the wall tissue weakens. In other words, they did not find evidence to support the notion that *global* wall weakening (drop in failure tension) was the cause of rupture. The current study

proposes to study whether the latter is the culprit – that is, could AAA rupture be caused by abnormal elevation in the pressure induced wall tension?

The objective of this study is to test the hypothesis that *Pressure induced wall tension in ruptured aneurysms is higher than pressure induced wall tension in unruptured aneurysms*. The 13 wholly harvested AAA (four ruptured and nine un-ruptured) that were reported upon in Raghavan et al.'s study will be used for this study as well. While this hypothesis has been studied and reported upon earlier [11, 12], the uniqueness of this investigation is in the level of detail available to us on the AAA involved in this study. For the first time, we have regionally varying measured wall thickness and regionally varying wall properties – data, which has never been available outside of this group of specimens. Since the geometric information is also available, this study will permit for the first time, a more rigorous estimation of the condition of the AAA wall in order to test of this hypothesis – albeit with a small study population.

CHAPTER 2: MATERIALS AND METHODS

There were three primary steps in the methodology to test the hypothesis. The primary steps in Figure 6 will be expanded in later sections. The first step was the three dimensional geometric reconstruction of each aneurysm, the second step was to incorporate the measured data into the computational model, and the last step was to perform the Finite Element Analysis (FEA) with additional indices derived from stress analysis results.

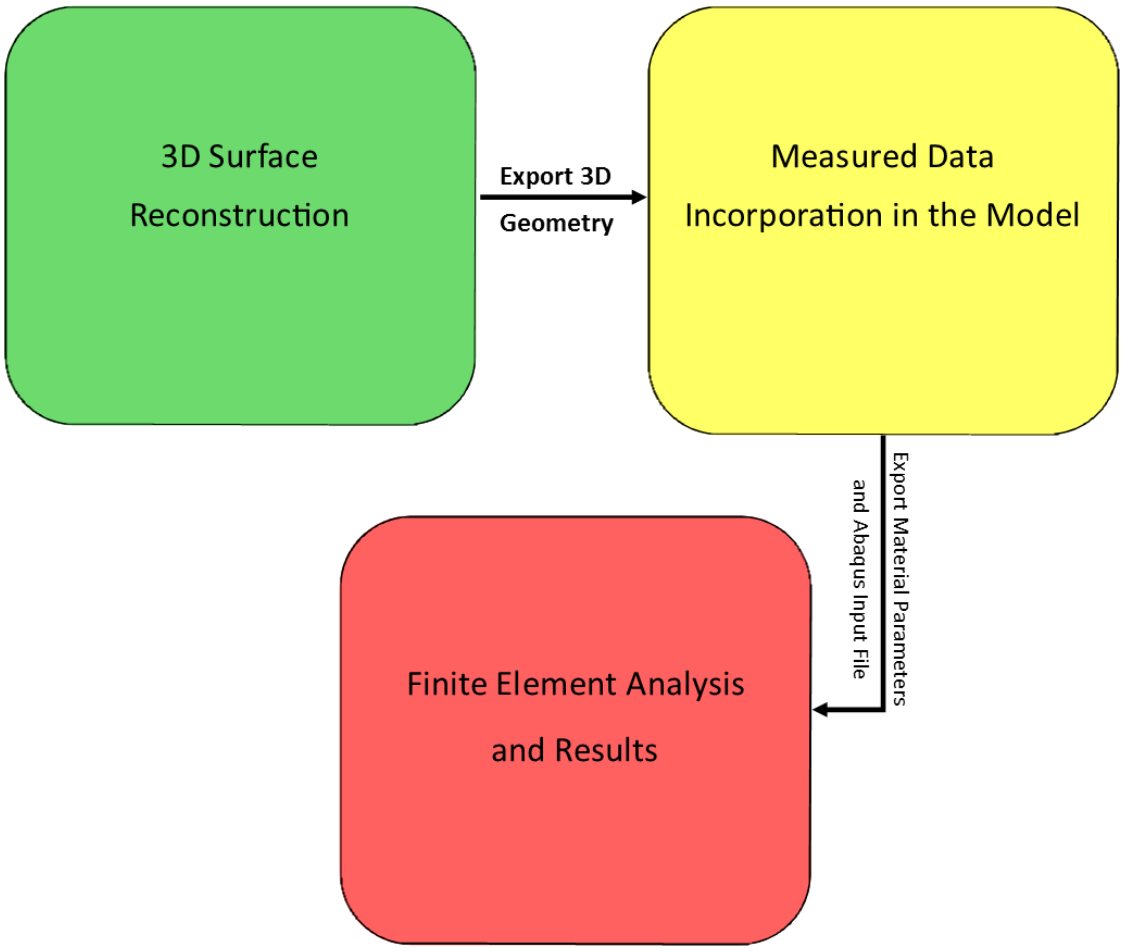

Figure 6: Summary of the methods used to reconstruct the aneurysm geometry, input measured data and run finite element analysis.

All thirteen aneurysms used the same methods and there were four ruptured aneurysms and nine unruptured aneurysms labeled A1 – A13 (Ruptured A1-A4, Unruptured A5-A13). The methods will track aneurysm 11 throughout the entire process of reconstruction.

Step 1: 3D Surface Reconstruction Summary

Traditional imaging modalities were unavailable for the reconstruction of the surface geometry of all the post-mortem aneurysms. The most prevalent method for geometric reconstructions of aneurysms use cross sectional data from computed tomography (CT) scans. The available data set that was available for reconstruction consisted of digital images that captured the hull geometry of each aneurysm.

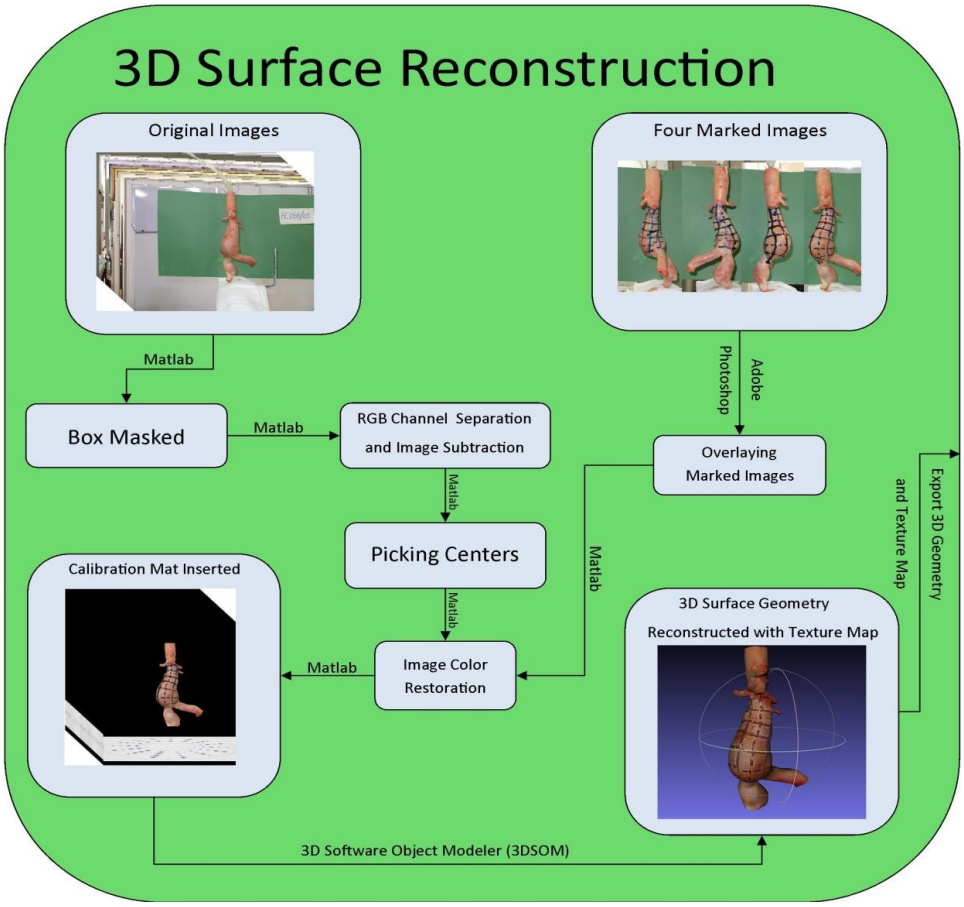

Figure 7: *Geometric reconstruction step with image processing, geometric reconstruction and texture map generation using various software.*

A wide range of techniques were used to convert two dimensional digital camera images into a three dimensional reconstructed surface. Figure 7 is a detailed flow chart of all the intermediate steps taken to perform the 3D reconstruction. Adobe Photoshop and custom Matlab scripts aided in the preparation of the input files for the 3D Software Object Modeler (3DSOM) software package.

Shape-From-Silhouette (SFS) through voxel carving has been used to represent surface geometries from two dimensional data sets, reverse engineering applications [30, 31] and for presenting electronic galleries of priceless artifacts [30, 32]. SFS utilizes multiple silhouettes of objects oriented in space with known markers to reconstruct the surface geometry. 3D Software Object Modeler (3DSOM) software implements this technique based on the optical positioning of the object in relation to a calibration mat. The calibration mat in itself gives distance and angle information back to the software to calculate the positions of the 2D silhouette slices in 3D space [32]. Figure 7 represents the entire 3D surface geometry reconstruction process with the intermediate steps explicitly described.

Image Segmentation

The original digital images were taken in front of a green background seen in Figure 8. This allows for the use of basic digital image processing algorithms to isolate the object (AAA) from the green background. The digital images were taken with a digital camera with a raster size of 2592 by 1944 pixels [33]. Most digital color images that are taken have three distinct color channels (Red, Green and Blue) which utilize color mixing to represent a single color perceived by the human eye [33]. Each digital image in the original set is a three dimensional matrix with a size of 2592 by 1944 by 3 (RGB channels).

Each pixel location has a value from 0 to 255 and populate the three dimensional matrix with integer data. In a gray scale image the brightest value ‘255’ is white and the dimmest value is ‘0’. It is computationally expensive to process the entire digital image when only considering the aneurysm as the object of interest as it would be unnecessary to capture the background information. The first step is to create a 'box mask'. The box mask is defined by two points that isolate the object with a rectangle. All pixel color values outside of this rectangle are assigned a zero value Figure 8. This is a very simple way to save time, disk memory and computational costs.

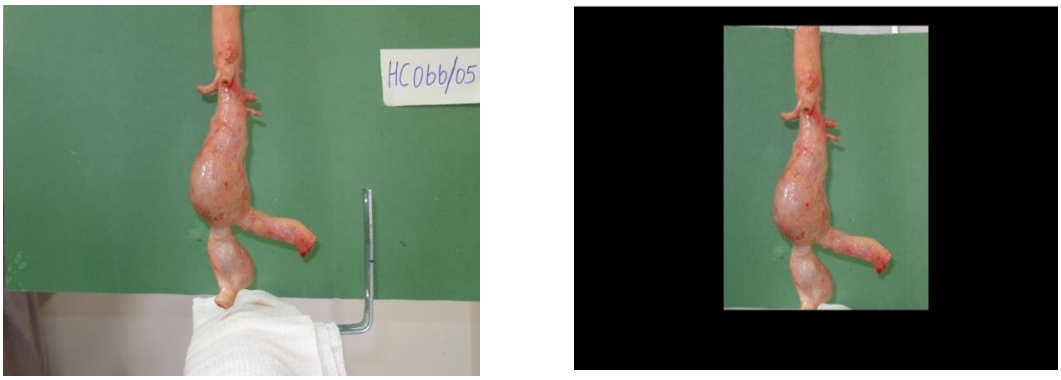

Figure 8: *Original Sample Image on the Left and Box masked image on the Right.*

Figure 9 displays all of the color channels decomposed into separate color channels. The red channel displays the aneurysm the brightest because of the red pigmentation. The green channel displays the background the brightest because it is green. The aneurysm object is segmented from the background by subtracting the green channel image from the red channel image in each corresponding pixel location using simple matrix subtraction. The isolation results in the aneurysm object having positive pixel values while the background

consists of having negative pixel values. The negative values are simply filtered out to become a value of zero representing black.

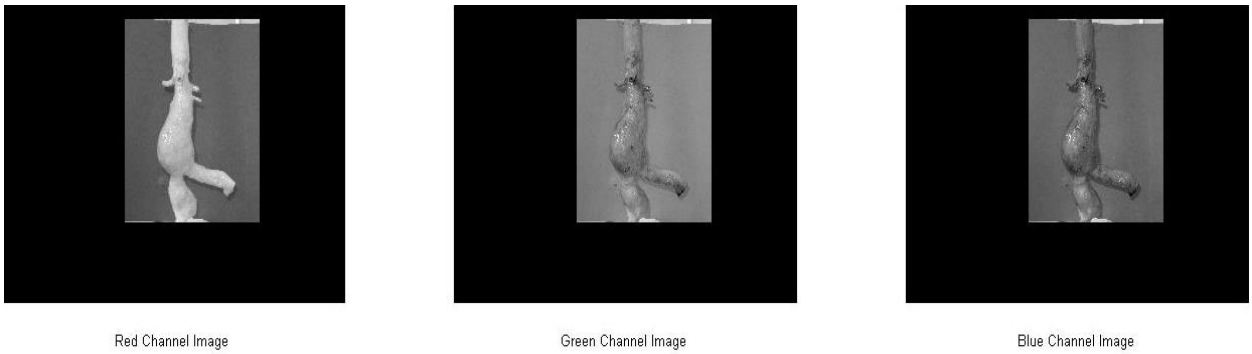

Figure 9: *Decomposed image, red channel (left), green channel (center), and blue channel (right).*

The image that isolates the object is then converted into a binary image (where the value 1 is white and 0 is black). The binary image is transformed by giving all negative pixel values a '0' value while giving all positive pixel value a value of '1'. The binary image seen in Figure 10 can also be used an image mask.

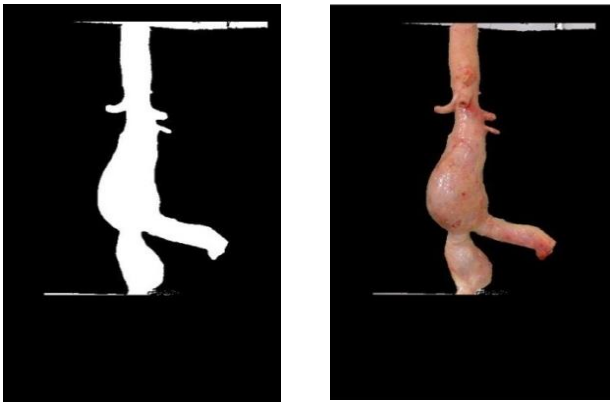

Figure 10: *Binary image mask (left) and recomposed image (right).*

The mask is multiplied (indicial multiplication) to each original RGB channel from the original image and the image is recombined to salvage the color data (Figure 10). Any black value (zero) multiplied by the pixel position in the original image will result in black, and any white value (1) multiplied by the pixel position in the original image will result in the original image color (for three separate channels and then recombined). Although there are some artifacts left in the masked image, they are automatically eliminated out of the image with the integrated image masking found in 3D Software Object Modeler (3DSOM).

For each aneurysm digital image data set, there are four images that were marked with blue and black dye. The digital images with markings was taken after the original digital image set was taken. The marked images were taken in the anterior, posterior, left and right views of the aneurysm. Image registration techniques were attempted to fit the marked images to the original data set, but the algorithms were unable to fit the marked images onto the original data set appropriately.

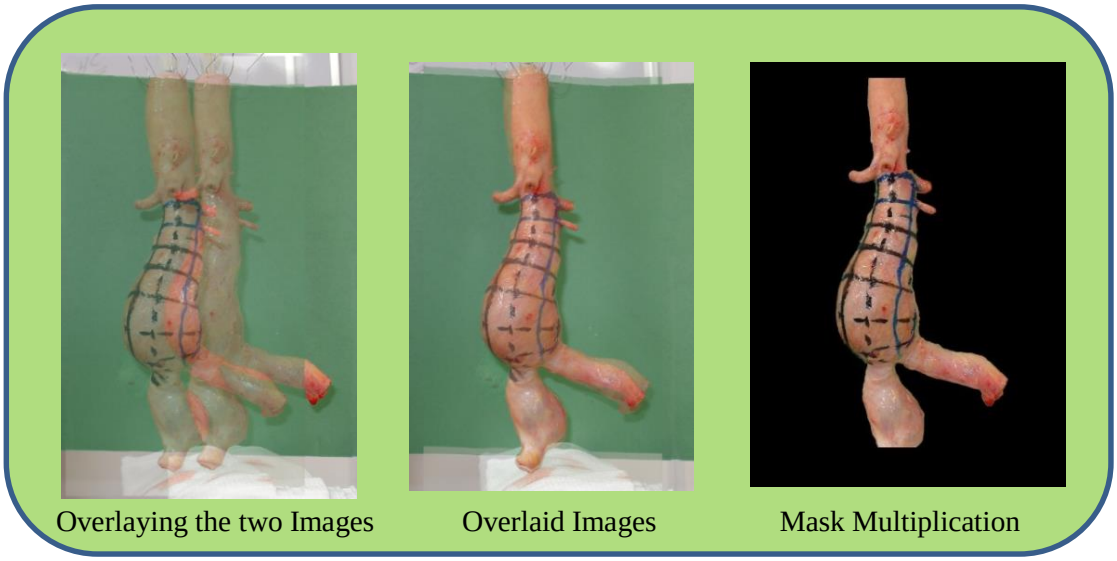

Figure 11: *Overlaying the two images (Left), Overlaid images (Center) and Mask Multiplication (Right) using Adobe Photoshop and Matlab.*

Adobe Photoshop was used to overlay the marked images onto the original image (seen in Figure 11). Simple image translation and image transformation were used to superimpose the marked images onto the original images. Although the iliac arteries are not completely lined up, the overlayed image is multilplied by the original mask to retain its original silhouette. The pigmentation and color data of the iliac arteries are not significant and can be ignored as they do not have any markings that map out thicknesses or material tests. The markings are key component in how the measured data is inputted on to the surface geometry and will be described in further detail in a later section.

Calibration Mat

The input images for 3DSOM are usually taken with a calibration mat (Figure 12). However, these digital images were taken before this method was implemented. A modified calibration mat (Figure 12) has a compass inserted within the 3DSOM mat to ensure accurate rotation of the mat.

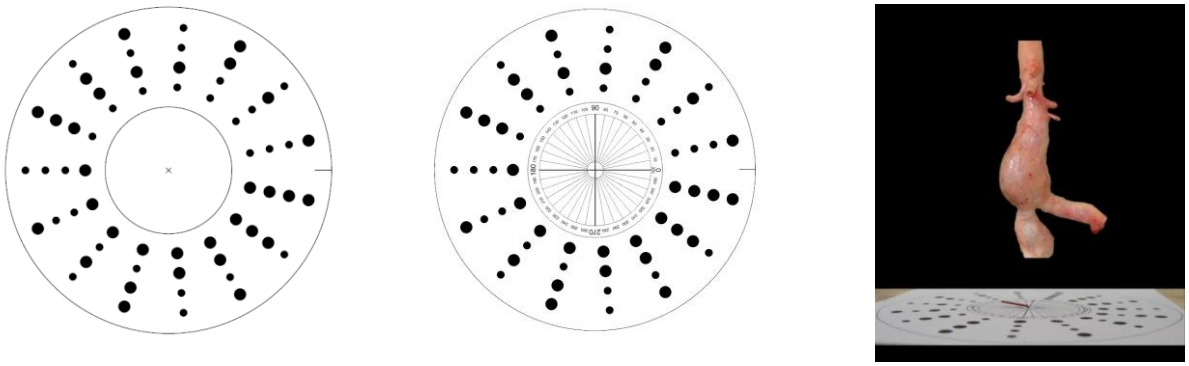

Figure 12: *Original calibration mat (left), Modified calibration mat (right), Recombined image with calibration mat inserted (right).*

Thirty-six images were taken of the calibration mat in 10^{o} increments similar to how the aneurysms were photographed and the calibration mat was photographed with a hybrid digital camera (to minimize blurring of the calibration mat). The calibration mats were inserted at the center of each aneurysm image (Figure 12). Automated algorithms to calculate the center of each aneurysm were attempted, but were insufficient in capturing the centers with reasonable accuracy. The centers were found manually by picking a single point on the neck of the aneurysm with a simple Matlab [34] batch script (to load images and pick points). After all of the centers were found, the calibration mat was inserted to each masked aneurysm image (Figure 12) in the same batch processing script.

Surface Reconstruction with 3DSOM

The masked images with the calibration mats were imported into the 3DSOM viewer. Figure 13 represents all of the steps within the 3DSOM surface reconstruction steps. Each image is automatically masked to remove any artifacts that may be present in the geometry.

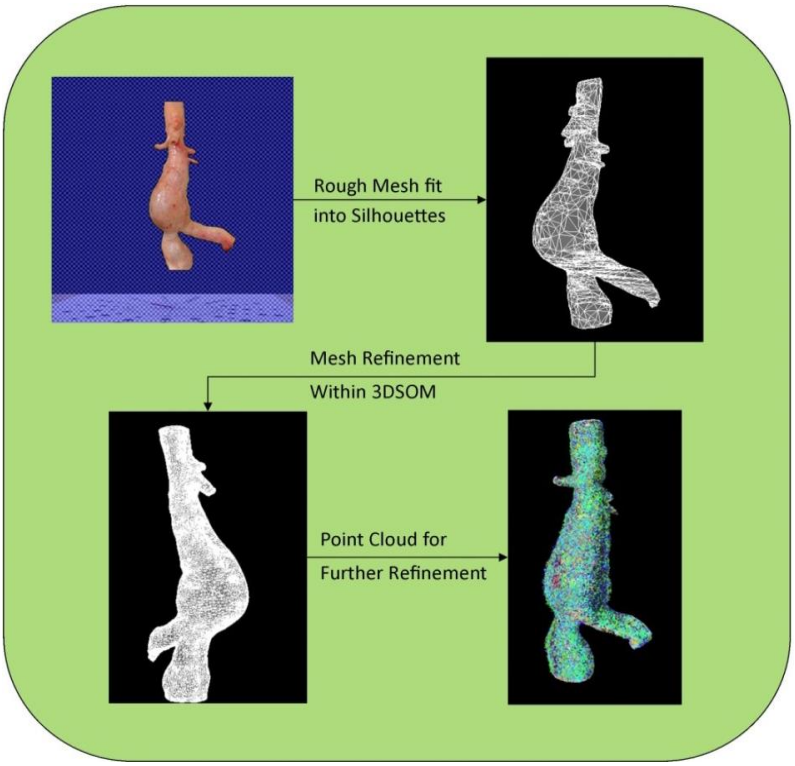

Figure 13: *3DSOM reconstruction steps using a rough mesh, refined/smoothed mesh and a point cloud.*

An initial rough mesh is fit within the silhouettes of the image set. Options are available on how many initial elements the rough mesh should have, how much surface error or silhouette error is allowed, and additional smoothing options after the rough mesh is generated [32]. The mesh can be further refined by specifying the number of nodes and elements that should be fit within the rough mesh.

Verification of Reconstruction Method

To determine the precision and accuracy of the reconstruction method, a sample reconstruction test was performed. The test image set included a rectangle with the calibration mat inserted in 10^{o} increments similar to what was done with the aneurysm images.

Theoretically, the reconstructed rectangles would reconstruct a cylinder because the images and calibration mat are being revolved about the center axis of the object.

The sample set includes only side views of the rectangles and no top views or bottom views. This was done purposefully to mimic the aneurysm data set and to validate the method being used. The 'top view' is seen in Figure 14 as a circle and the reconstruction of a 3D cylinder is an acceptable approximation of the two dimensional image set.

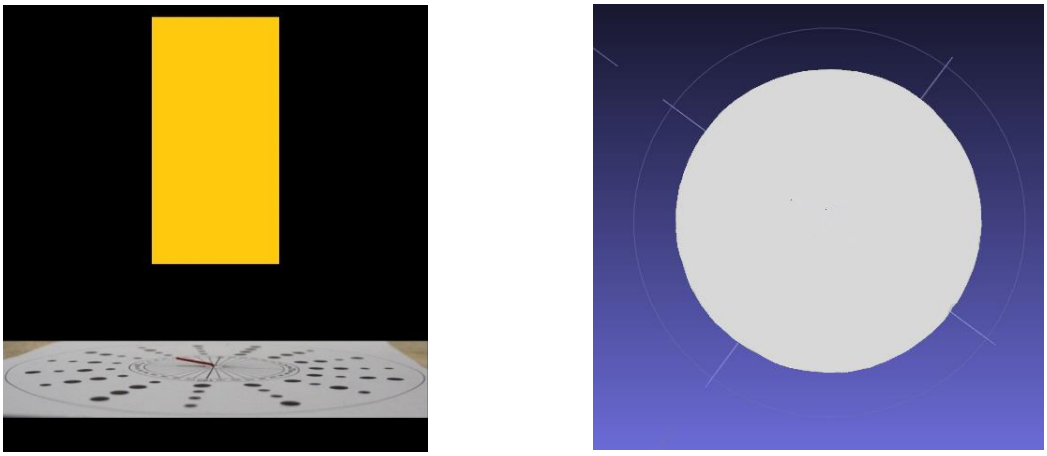

Figure 14: *Test cylinder with calibration mat (left) and reconstructed cylinder top view (right).*

Texture Map Generation

3DSOM has the necessary and important capability of generating a texture map. Texture maps relay color information from the original digital images to the 3D reconstructed surface [35]. These texture maps relay thickness information and material properties information from the 3D surface geometry to the finite element model. Four images were chosen as the highest priority for the texture map generation. These four images have the markings for where the material properties and thicknesses are located. Figure 15 captures the

texture map being wrapped around the three dimensional surface geometry. After the texture map was generated, the surface geometry and texture map were exported into Meshlab [2].

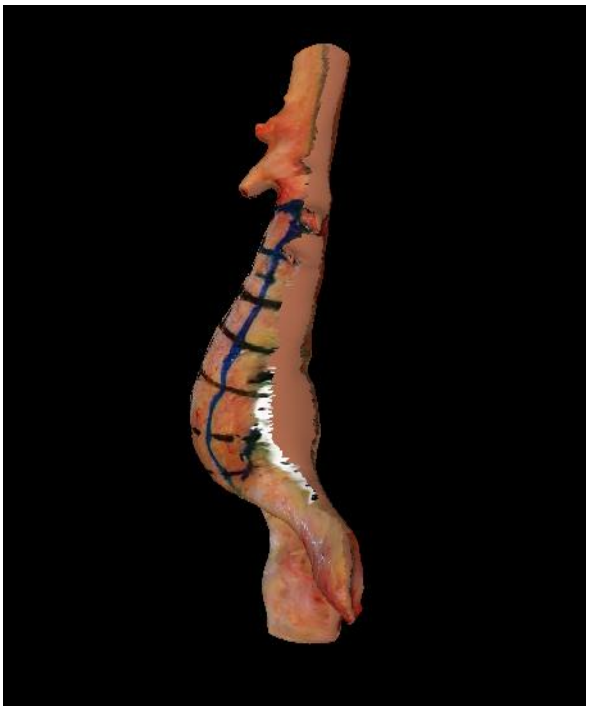

Figure 15: *Texture map reconstruction on the surface mesh geometry.*

Step 2: Measured Data Incorporation

The surface geometry and texture data were used to input measured wall thicknesses, material properties coefficients and failure properties. Meshlab [2] was used to refine the mesh and pick points on the surface of the mesh with the texture map, Rhinoceros [3] was utilized for mesh cutting of branching arteries and the proximal/distal ends of the aneurysm, and Matlab scripts were written for the interpolation method.

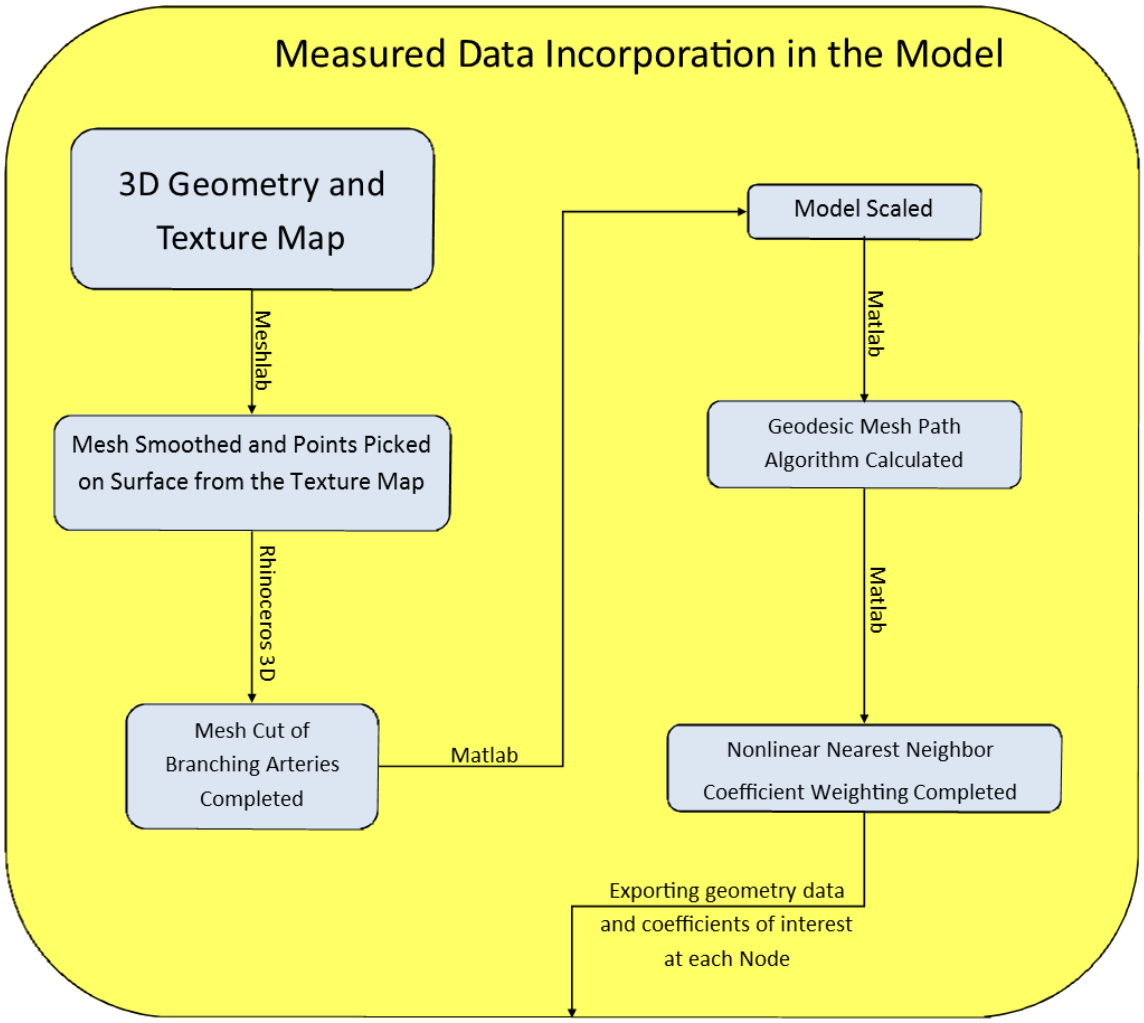

Figure 16: *Step 2 overview of how the measured data was incorporated into the finite element model.*

Marked Image Maps and Points Picking

Four marked image maps denote measured thicknesses and uniaxial extension test strips in the anterior, posterior, left and right views of each aneurysm. Figure 17 gives an example of the 'left view', the drawn up rectangular box represents the strips for uniaxial extension testing and the numbers/points correspond to thicknesses in millimeters (mm).

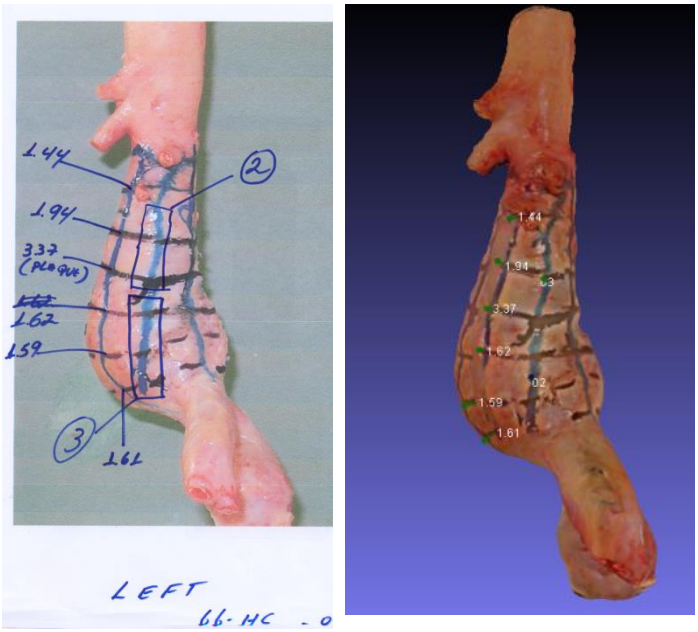

Figure 17: *Marked images with thicknesses and material specimen locations (left), picked points in Meshlab (right).*

Points were manually picked using an open source 3D model visualizer known as Meshlab [2]. The reconstructed surface geometry and the texture map were imported into Meshlab and points were picked manually as seen in Figure 17. All thickness locations and material properties locations were exported and then imported into Matlab. Each point that was picked was assigned a three dimensional Cartesian coordinate on the surface of the mesh and assigned a scalar based on thickness or material coefficients. The Cartesian coordinates of a picked point was then translated into a specific node based on its proximity to the node in the entire mesh.

Mesh Cutting and Smoothing

The proximal/distal ends and the branching arteries were cut in Rhinoceros 3D (Figure 18). Cutting planes are generated by using two orthogonal views of the aneurysm. The mesh was then split using the built in mesh splitting function and the mesh was truncated.

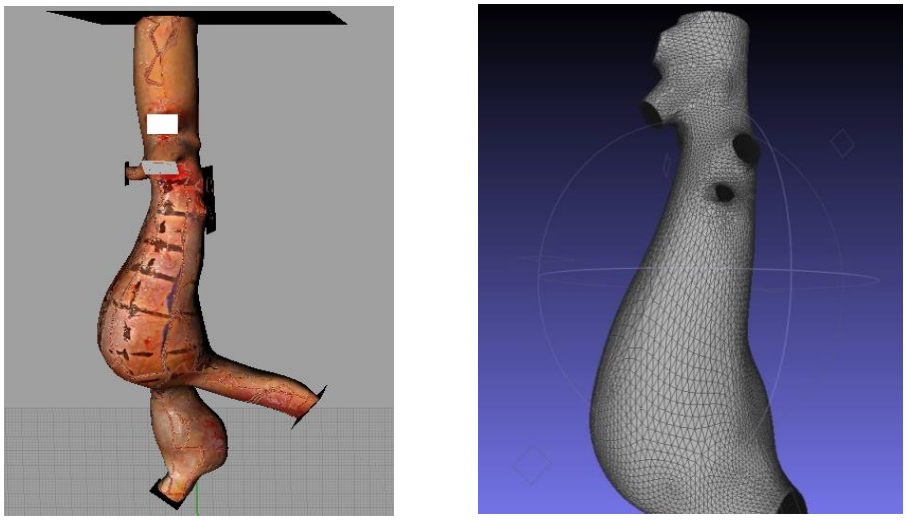

Figure 18: Mesh cutting planes (left) in Rhinoceros 3D, Laplacian surface preserved smoothing in Meshlab (right) [2, 3]

After the mesh is cut, additional smoothing operations are performed. The cut mesh geometry is exported from Rhinoceros and imported into Meshlab. The mesh is smoothed in Meshlab using a surface-preserving Laplacian smoothing algorithm (Figure 18). There is no additional mesh manipulations performed after this step has been completed and the smoothed cut mesh data is exported and then imported into Matlab.

Model Scaling

Inserting the calibration mat with an arbitrary size alters the global coordinates and overall unit dimensions. The model is scaled to the desired unit of measurement (centimeters).

Model units refer to the arbitrary units used in the 3D mesh and pixel units refer to the pixel distances found in the original image.

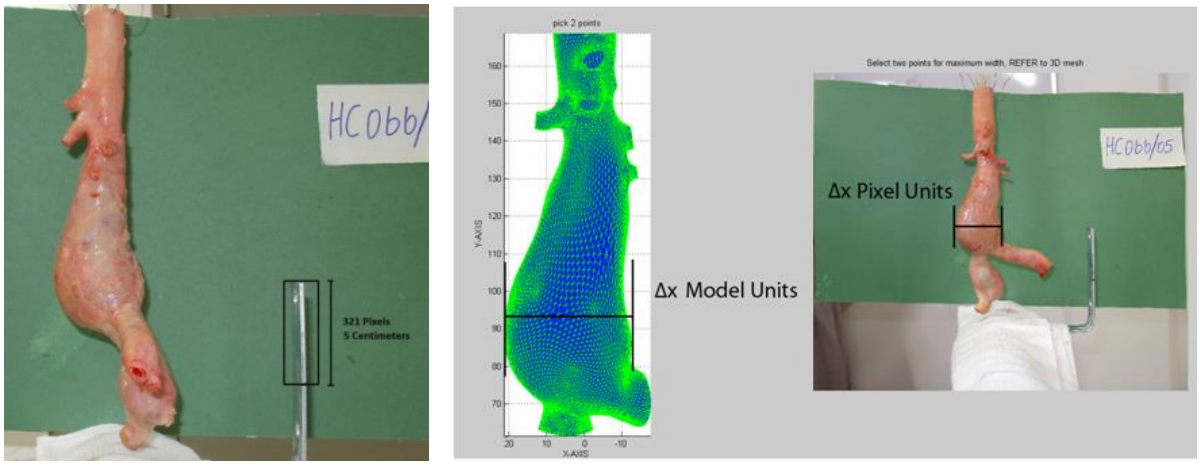

Figure 19: *Original image with scale (left), 3D model and original image reference scale (right).*

A batch processing script was created to scale down the model from model units into scaled units. Figure 19 shows the known distance of 5 centimeters in the image which translates to 321 pixels. Figure 19 shows the side by side points picking from the 3D mesh and the image to get the model units. Points are picked ten times and the average is taken as the scaling factor. Equation 3 shows how these units are converted into the desired unit of centimeters. After the scaling factor is determined, the model units are multiplied by the scaling factor to give the aneurysm meaningful units of measurement.

Equation 3: *Scaling Factor Calculations*

$$Scaling\ Factor = \left(\frac{\Delta x\ Pixels}{\Delta x\ Model\ Units} * \frac{Known\ Distance}{Pixel\ Reference}\right)$$

$$Scaled\ Units = (Model\ x, y, and\ z\ units) * Scaling\ Factor$$

Material Model Coefficients

Each aneurysm wall specimen taken from the aneurysm was subject to uniaxial extension testing [4]. All material specimens were oriented in the longitudinal direction and not the circumferential direction. The data collected includes displacement and the load at each displacement. Figure 20 shows a single extension test that was curve fitted using the material model previously stated.

The two coefficients are used later as scalars to be interpolated on the surface as well as material model inputs (describing the material curve) for Finite Element Analysis. All material specimens that had successful uniaxial extension tests were assigned an alpha and beta coefficient. Most of the curve fitting and the extraction of the alpha and beta coefficients were performed prior to incorporating these coefficients into the finite element model.

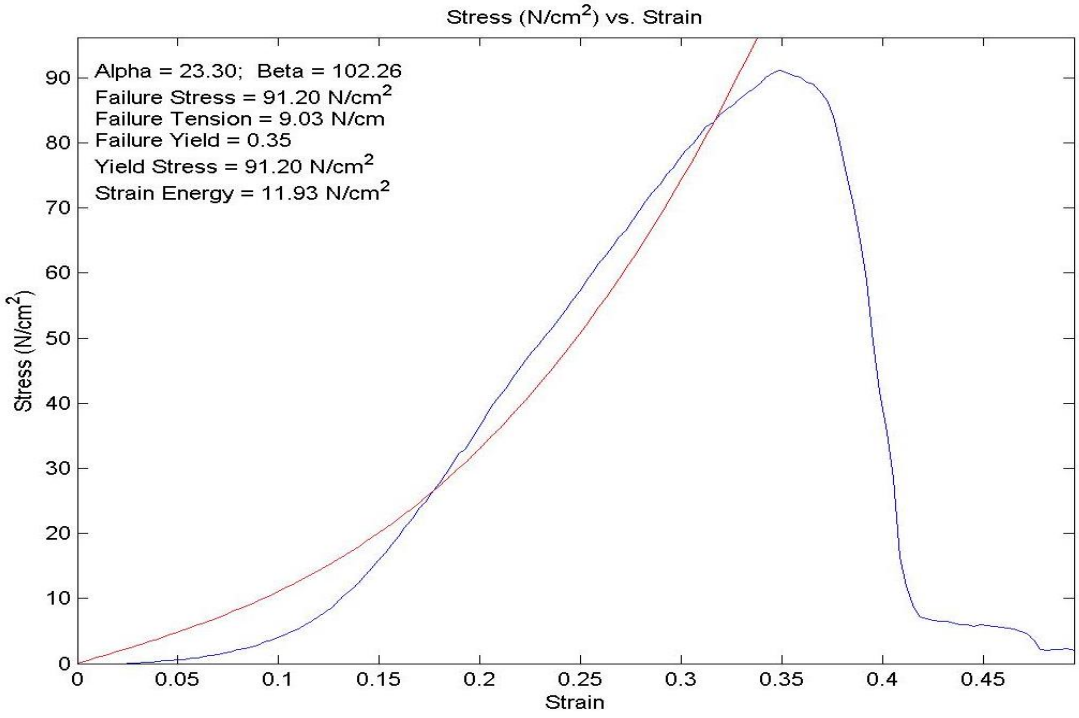

Figure 20: *Original uniaxial extension test with curve fitting to material model found in Equation 2.*

Geodesic Mesh Path Algorithm

Geodesic distances on the surface of a mesh are usually defined as the shortest path distance between two points on a surface. The general motivation behind the geodesic mesh path algorithm was to minimize the mesh distance calculations. Rather than calculating distance between two nodes, the distances were calculated from one central node (node with known scalar value) to all nodes in the mesh.

The reconstructed mesh surface is defined by nodes and element connectivity. However, there are only a few scalars defined for the entire mesh surface. Scalars are defined by the measured wall thicknesses, alpha coefficients, beta coefficients and failure properties (stress, tension). Known nodes that have known scalar values are defined by their respective Cartesian coordinates on the reconstructed mesh surface. These known nodes are defined as *epicenters*, while the node connectivity per iteration is defined as an *impact zone n* (n iterations). The idea is to create concentric impact zones about the epicenter, and update the distances after each iteration. The radius in the concentric circle on a surface is the shortest path on the mesh surface which is constrained by element connectivity.

The distances are calculated after each iteration and the distances are updated for each iteration. Equation 4 shows this explicitly by essentially generating a circle of node neighbors around the epicenter and will generate node neighbors around each impact zone. Each node in the node neighbor impact zone has the Euclidean distance calculated to the previous node set and the minimal distance is chosen. Any node in a given impact set is not reused for the iterations to follow.

Equation 4: *Distance Matrix Algorithm*

$$I_n \in TRI^{i,3}\ ;\ \sum I_{n-1} \notin I_n;$$

$$d_{i,j} = \sum_{j=1}^{j} \sum_{n=2}^{n} min \left| \sqrt{I_n^2 - I_{n-1}^2} \right|$$

$$I_n = Nodes\ in\ Impact\ xyz, TRI = Element\ Connectivity;\ d_{i,j} = distances;$$

$$i = nodes\ in\ mesh, j = columns\ (maximum\ number\ of\ epicenters), n = iterations$$

Geodesic Distance Weighted Interpolation Method

In the previous section, a method to calculate geodesic mesh path distances was defined. Essentially, all nodes are defined as distances to a known node with a scalar value. A subset of the Geodesic distance matrix is taken so that the distance is minimized for four nodes to four known scalar nodes. The interpolation method consists of ranking these four distances nonlinearly based on their proximity to a known node.

There is a single distance matrix $d_{i,j}$ that includes i nodal distances between all nodes i to known scalar nodes and value t_j. The first column $d_{i,1}$ refers to the scalar value t_1 and all of the entries i would refer to the distances from the node to the node of the scalar value t_1 (distance at node t_1 is set to 0.01). The minimized distance matrices $md_{i,j}$ are an ordered subset (four distances min to max) of $d_{i,j}$ that include the scalar t_j associated with $md_{i,j}$. The $md_{i,j}$ matrix represents the four lowest distances to known scalar values t_j.

The nonlinear component of the weighting system rewards the lowest minimized distance to its scalar with the highest weight based on their proportion of contribution. The first weight is defined as the first pre-weight, and the leftover proportion is considered to be the contribution from the rest of the pre-weights. Nodes that are closer to the known scalar value nodes are assigned highest weight as they are to have greater influence from those scalars. After the weights are found they are multiplied by the scalar value t_j associated with column j.

Equation 5: *Pre-weights and Nonlinear Weighting of Coefficients.*

$$D = \sum_{j=1}^{4} md_{i,j}$$

$$\boldsymbol{w_{i,1} = 1 - \frac{md_{i,1}}{D}}$$

$$\boldsymbol{w_{i,2} = \left(1 - \frac{md_{i,2}}{D}\right)(1 - w_{i,1})}$$

$$\boldsymbol{w_{i,3} = \left(1 - \frac{md_{i,3}}{D}\right)(1 - w_{i,1})(1 - w_{i,2})}$$

$$\boldsymbol{w_{i,4} = \left(1 - \frac{md_{i,4}}{D}\right)(1 - w_{i,1})(1 - w_{i,2})(1 - w_{i,3})}$$

$$Interpolated\ Value_i = \sum_{j=1}^{4} t_j \times w_{i,j}$$

Step 3: Computational Analysis

The finalized surface geometry (nodes and elements information) and material coefficients are imported into an Abaqus input file for computational analysis. A Matlab script exports Abaqus input files with varying material properties, Abaqus calculates the solution of the input files, and the results are further post-processed in Matlab and the data is exported into Tecplot [34, 36, 37].

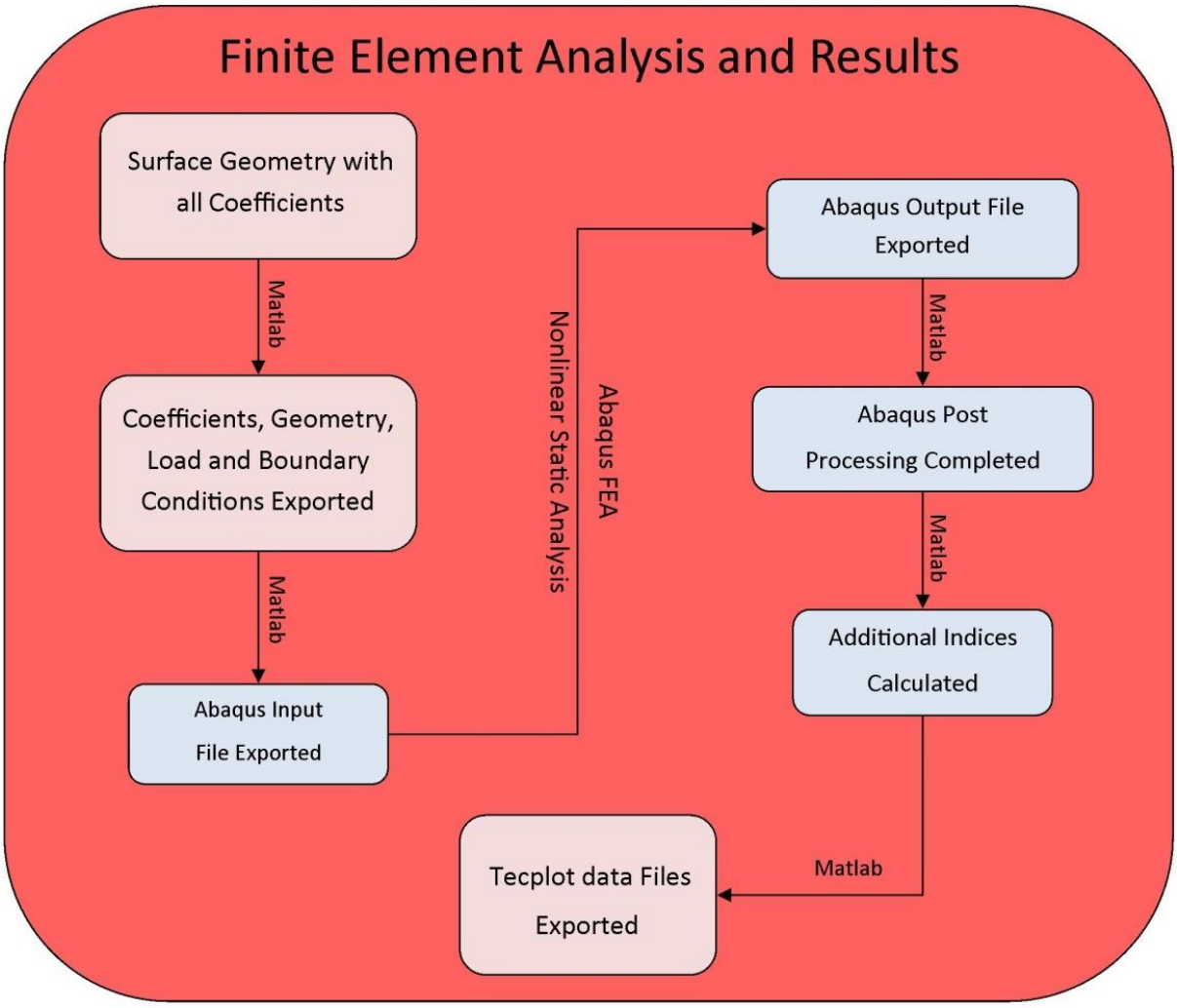

Figure 21: *Step 3, Finite element analysis, post-processing and data viewing.*

Finite Element Material Models

Finite Element Stress Analysis is computed using Abaqus. There were eight different FE Models created with four different material properties (Table 3). These eight FE models are indicative of the stress analysis that has been previously seen in literature [10-12, 18-20, 22, 23, 26]. There are two major groups of models: Group A has the same wall thickness defined (taken by the mean of all known measured thicknesses) and Group B which has variable wall thicknesses (based on the weighted interpolation method described previously).

Each major group is subdivided into four different material models ranging from the simplest to most complex. The simplest material model, 'M1' is a linear elastic model that has an Elastic Modulus of 500 N/cm^2 and a Poisson's Ratio of 0.49 (effectively incompressible) [26]. The second material Model, 'M2' is a linear elastic model (E = 500 N/cm^2, mu = 0.49) with nonlinear geometry defined (NLGEOM). Model 'M3' utilizes a hyperelastic material model that was experimentally derived by Raghavan et al. [18] with a single alpha and beta coefficient describing the aneurysm (alpha and beta are determined by the mean of all known extensions test for the aneurysm). Model 'M4' is the heterogeneous material model which defines all elements with a different alpha and beta coefficient based on the weighted interpolation method.

Table 3: Finite Element Model Material Properties Parameters.

	Linear Elastic (mu and E)	**Non-Linear Geometry**	**Homogeneous Hyperelastic**	**Heterogeneous Hyperelastic**
Group A Model 1	●			
Group A Model 2	●	●		
Group A Model 3		●	●	
Group A Model 4		●		●
Group B Model 1	●			
Group B Model 2	●	●		
Group B Model 3		●	●	
Group B Model 4		●		●

Finite Element Model Boundary and Loading Conditions

Patient specific blood pressure was not available for each aneurysm. All FE Models were subject to an idealized physiological load of 120 mmHg. Loading units are converted to N/cm^2 which translates to about 1.60 N/cm^2. Stresses are reported in N/cm^2 as well. The load is applied as a distributed pressure load normal to each element face.

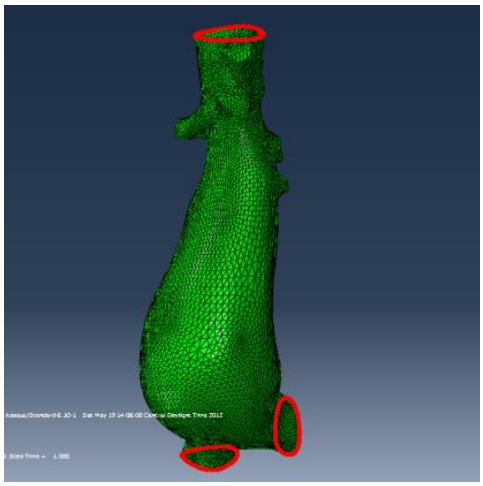

Figure 22: *Boundary Conditions*

The boundary nodes sets are nodes that are located on the proximal and distal ends of the aorta. Boundary node displacements are constrained in the x,y, and z directions and are not allowed to have any rotations about the x,y, and z axes (Figure 22). Abaqus Standard [37] was used to solve the solution using static linear and static nonlinear analysis.

Abaqus Post-Processing

After the analysis is completed for each model, Abaqus writes a data file that includes displacement information and stress information at each node. This file is imported into MATLAB and code has been written to import/export this data into the Tecplot viewer format

(Figure 23). This allows for clearer visualization of the stress distributions and other indices of interest (tension, principal stresses, thicknesses, material properties, and rupture potential index).

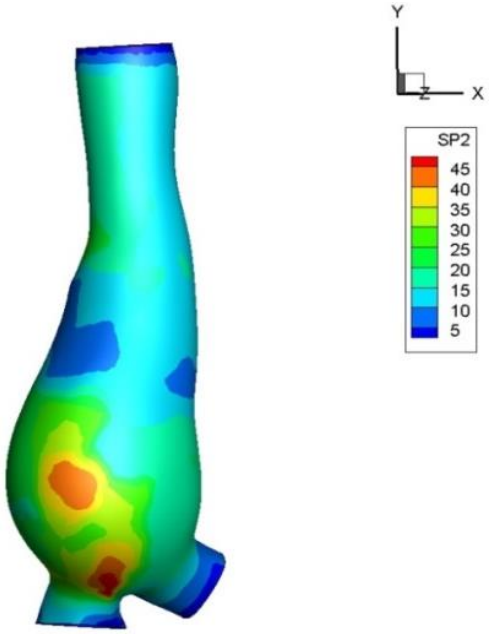

Figure 23: *Tecplot viewer of maximum principal stress.*

Displacement values are added to the original nodal locations to visualize the deformation that occurred after the maximum pressure load has been applied. The principal stresses and other stress indices are also assigned to each node as well. There are various indices that have been calculated in literature and will be further discussed later.

Post-Processing calculations are performed with basic mathematical operations seen in Equations 6 - 7. Tension was calculated by multiplying the surface area change proportion with thickness (same wall thickness or variable wall thickness) and the maximum principal stress at a given location (Equation 6).

Equation 6: *Tension Calculations*

$$Tension = Max\ Principal\ Stress \times Interpolated\ Thickness \times \frac{Surface\ Area\ Initial}{Surface\ Area\ Final}$$

In order to calculate the Rupture Potential Index (RPI) for tension and strength, the failure tension and failure strength must be known [23]. Failure tension and failure strength were experimental quantities (n~7 per aneurysm). Both failure tension and failure strength were interpolated on the mesh surface using the nonlinear nearest neighbor weighting of coefficients. After the interpolation was completed, the RPI was calculated for both stress and tension.

Equation 7: *Rupture Potential Index of Tension and Strength.*

$$RPI\ Tension = \frac{Tension}{Interpolated\ Failure\ Tension}$$

$$RPI\ Strength = \frac{Max\ Principal\ Stress}{Interpolated\ Failure\ Strength}$$

CHAPTER 3: RESULTS

Measured wall thicknesses and failure properties are presented as a reference to the overall properties of each aneurysm. The Tecplot plots display aneurysm 11 in the anterior and posterior orientations of the experimentally measure values with the interpolation results. In every plot the aneurysms are ordered as aneurysm 1 to aneurysm 13. The ruptured aneurysms are the first four in every data plot (A1 – A4) and the unruptured aneurysms are the rest of the aneurysms (A5 – A13).

The results with the highest model complexity (the BM4 model with variable wall thicknesses and heterogeneous material properties) will be presented first with box plots of tension, RPI tension, RPI strength and maximum principal stress along with tables summarizing the min (5^{th} percentile), median and maximum (95^{th}, percentile). Statistics will also be presented of the BM4 model along with other material models that were proposed in the methods section for completeness. An additional section of results for a less complex material model (the AM3 model with variable wall thicknesses and heterogeneous material properties) to compare with the material model with highest complexity. The last section will consist of Tecplot plots comparing the two material models side by side of the various indices that were presented earlier in the results section along with tables comparing the indices shown qualitatively.

Measured Failure Properties within the Population

There are three separate plots (Figure 24 – 26) of measured thickness, failure tension and failure stress derived from Equations 2a and 2b using force displacement data. These plots are representative of the experimental data collected for each aneurysm and give a quick glance at the aneurysm wall characteristics. Figure 25 represents the uniaxial wall failure tension scatter plot similar to Figure 5, but is ordered by the given aneurysm numbering system rather than by increasing diameter. Figure 26 represents the uniaxial failure stress in a scatter plot that is ordered using the same convention.

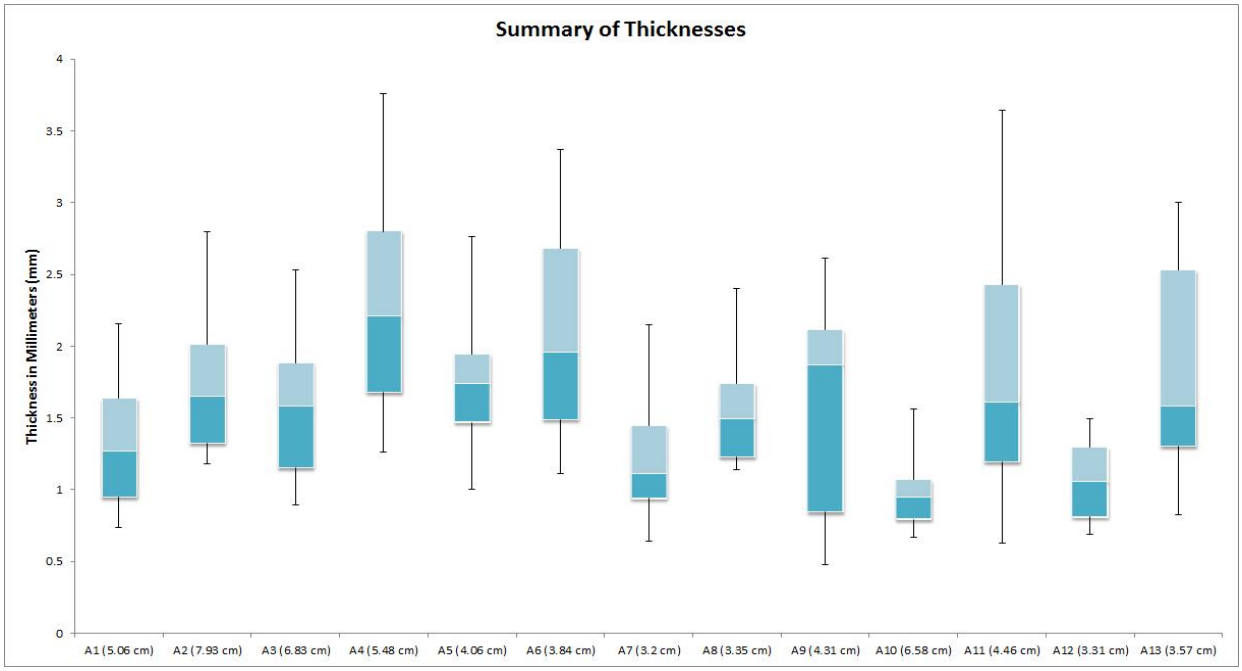

Figure 24: *Summary of measured thicknesses for all aneurysms in the population [4]*.

The ruptured aneurysms were on average found to be no weaker than the unruptured aneurysms in the same population for both cases of wall failure tension and wall failure stress [4, 16]. The thicknesses of the ruptured aneurysms were not found to be thinner than the unruptured aneurysms as well.

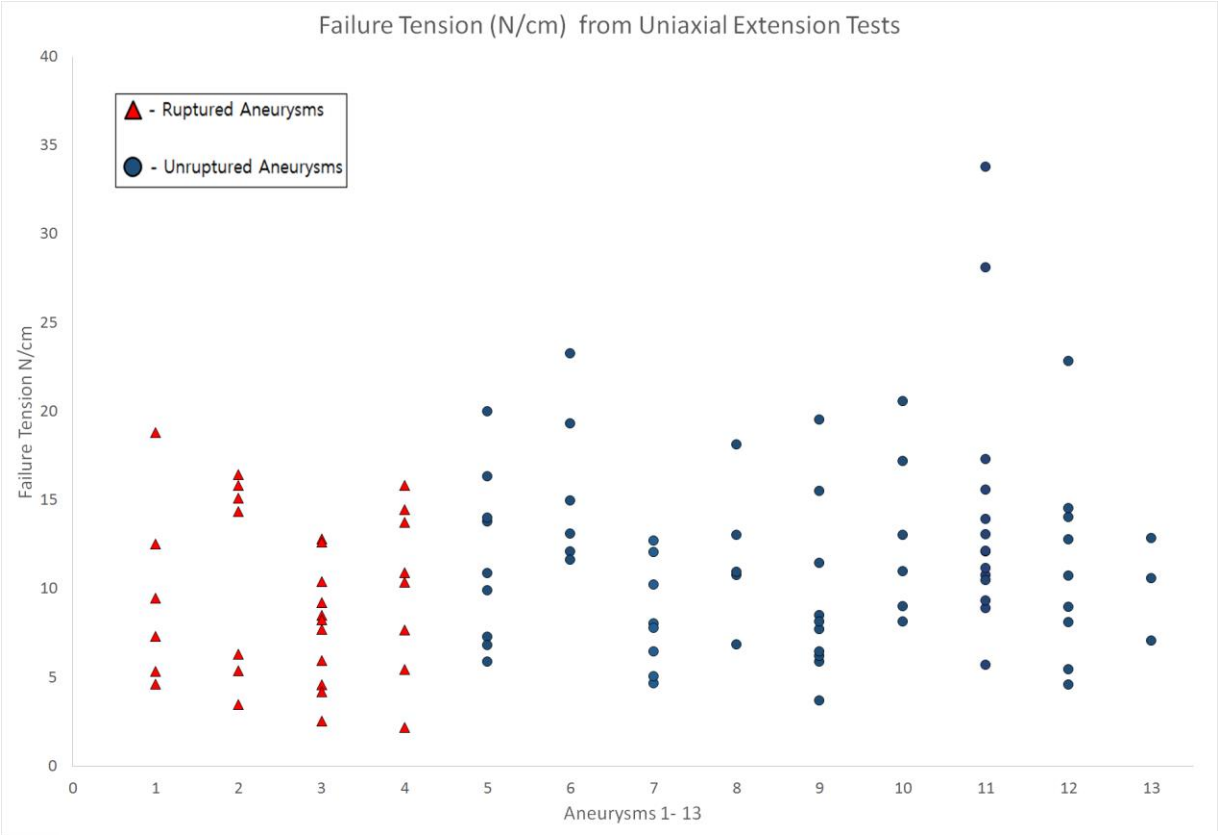

Figure 25: *Wall failure tension from uniaxial extension tests with ordered aneurysm numbers [4]*

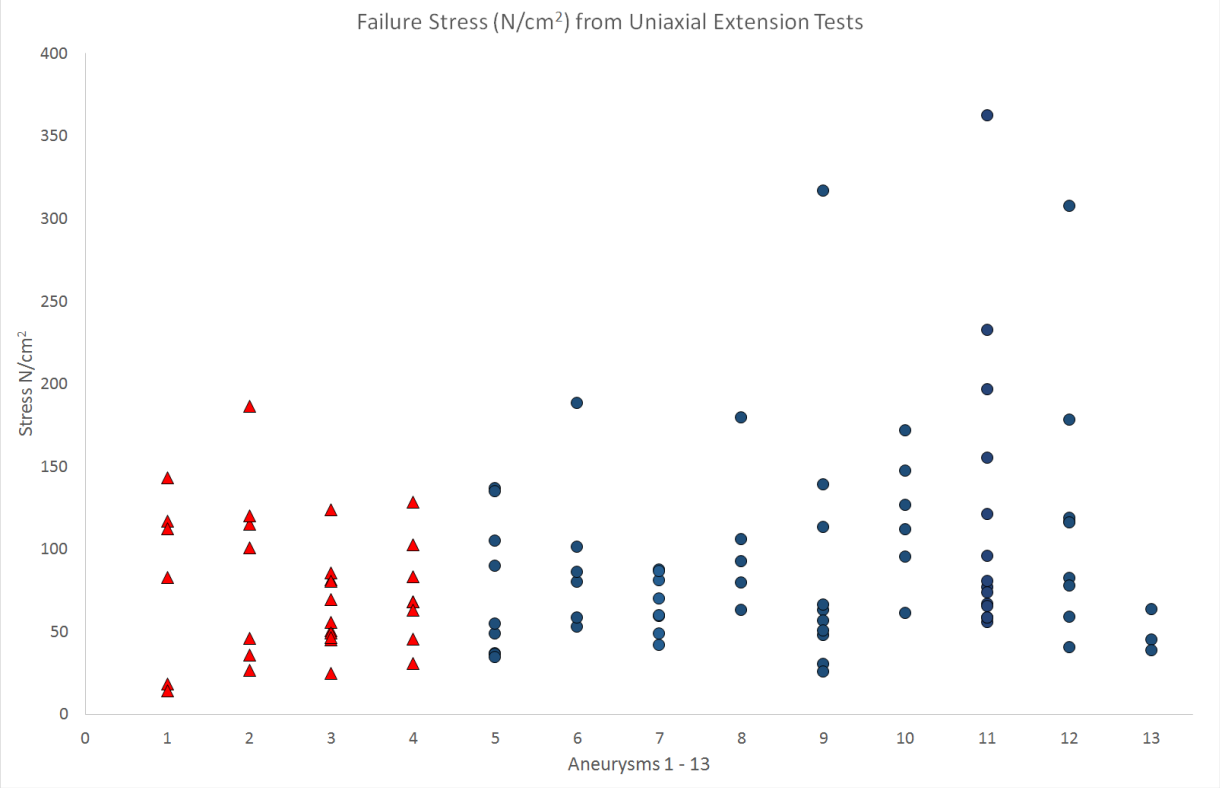

Figure 26: *Wall Failure Stress from uniaxial extension tests with ordered aneurysm numbers [4].*

Figure 27 displays the anterior and posterior regions of the aneurysm along with the original thickness values. The interpolated values prescribed by a nonlinear nearest neighbor weighting scheme fills all unknown values in a reasonable manner. There are no smooth color boundaries due to the interpolation being dependent on the mesh path.

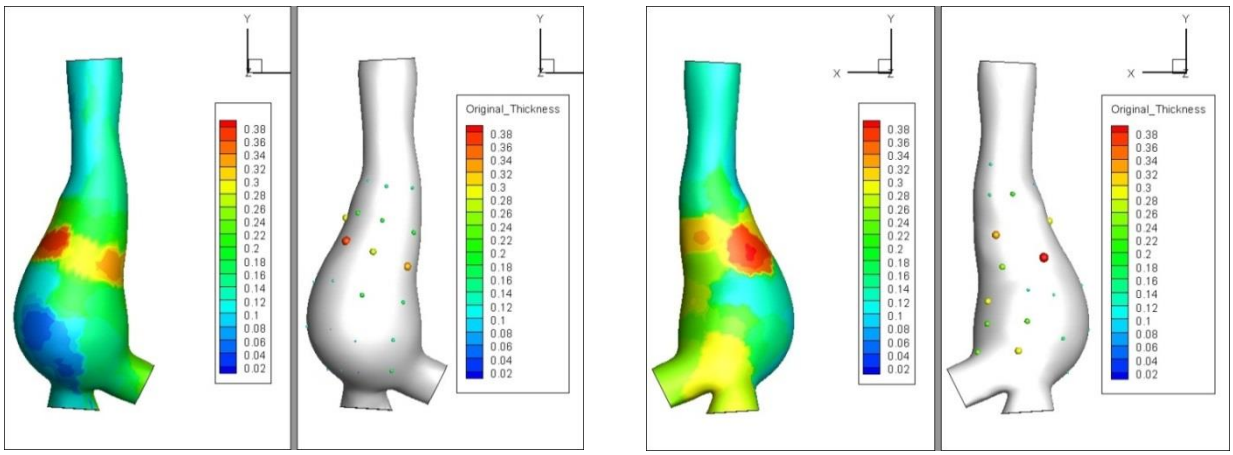

Figure 27: *Side by side interpolated thickness with original thickness Anterior view (left) and side by side interpolated thickness and original thickness Posterior view (right).*

The interpolation of the material properties (α, β coefficients, failure stress, failure tension) net similar qualitative results with varying values depending on the type of scalar value. Figure 28 displays the aneurysm in the anterior and posterior view and would represent all interpolations of material properties. The interpolation method does not allow any scalar on the surface to dip below or exceed any known scalar value for thicknesses, failure properties, and material coefficient values.

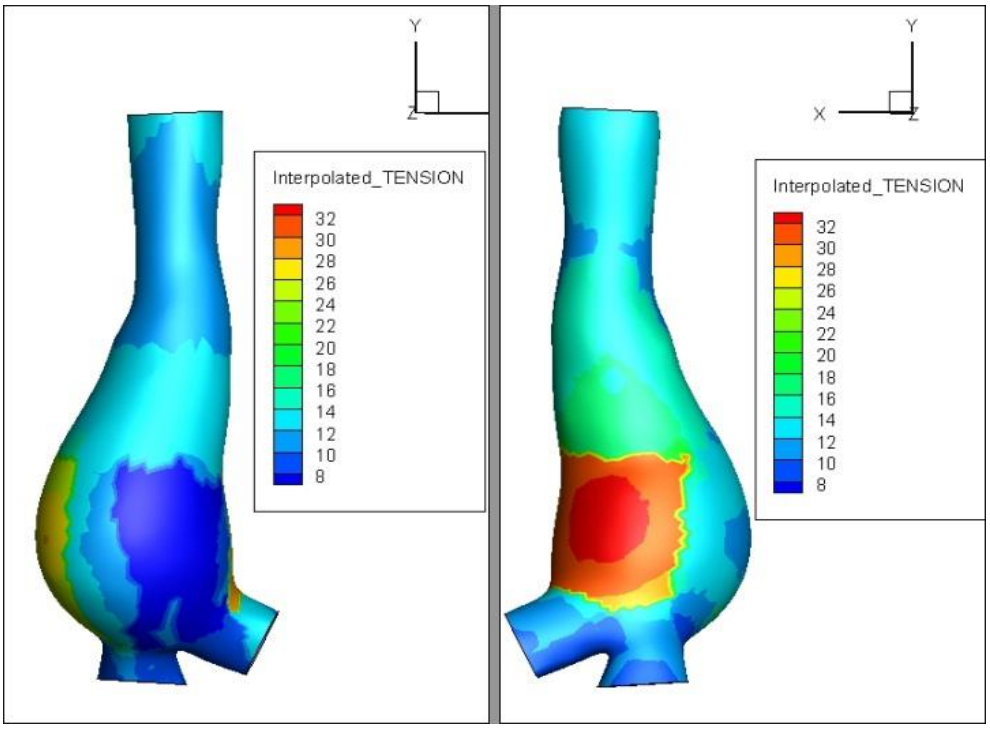

Figure 28: *Interpolated failure tension and material properties (qualitatively the same for all failure stress, alpha and beta coefficients with different scalar values).*

Results for the Most Complex Model (BM4)

Indices that are presented for the BM4 model include wall tension, maximum principal stress, RPI tension and RPI stress. The BM4 has the highest model complexity with variable wall thickness and heterogeneous material properties. Each plot also includes a table of the minimum index value (5th percentile), median and maximum value (95th percentile).

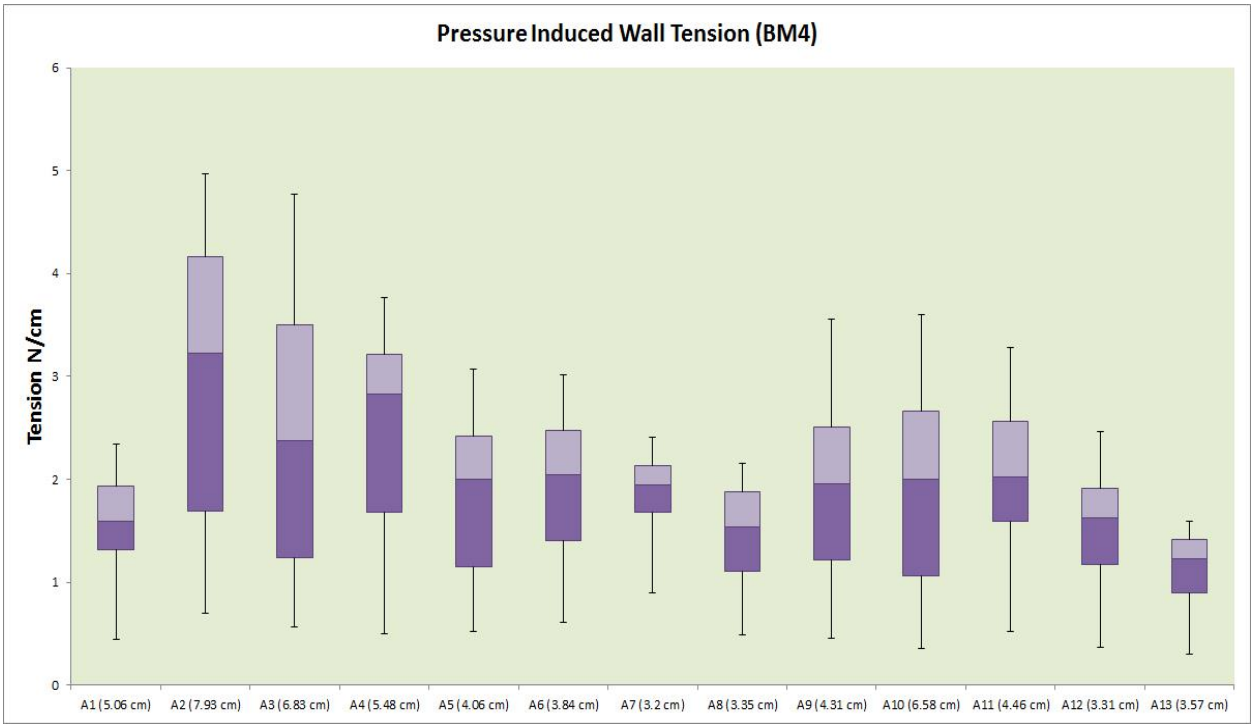

Figure 29: *Pressure induced wall tension box plot of all aneurysms, with variable wall thickness and variable hyperelastic material model material properties.*

Figure 29 - 30 represents the pressure induced wall tension and principal stresses (maximum principal stress) of the most complex model and Table 4 - 5 displays the exact values for the min, median and max for the corresponding figures.

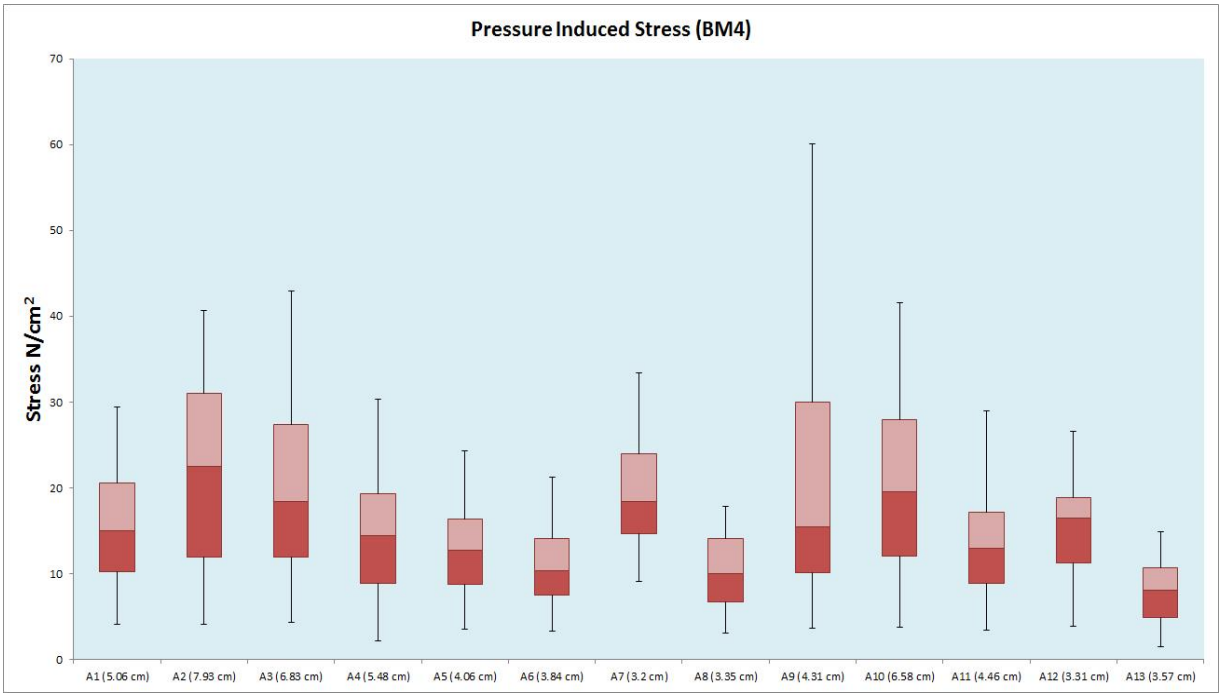

Figure 30: *Pressure induced maximum principal stress for the BM4 model for all aneurysms.*

Figure 31 represents the RPI wall tension for the most complex model. Figure 32 is a boxplot for the RPI wall strength for the most complex model. The RPI table is the combination of the RPI tension and RPI stress seen in table 6 to compare at a glance the RPI using two indices (tension and stress).

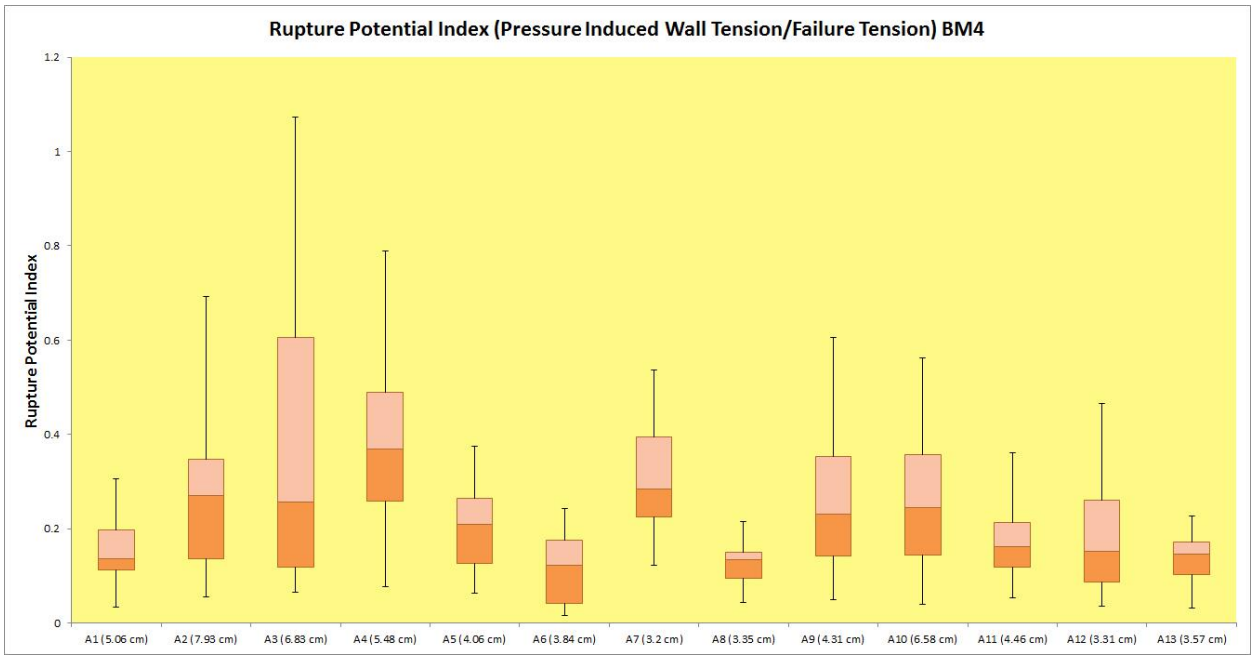

Figure 31: Rupture potential index for tension of the BM4 model.

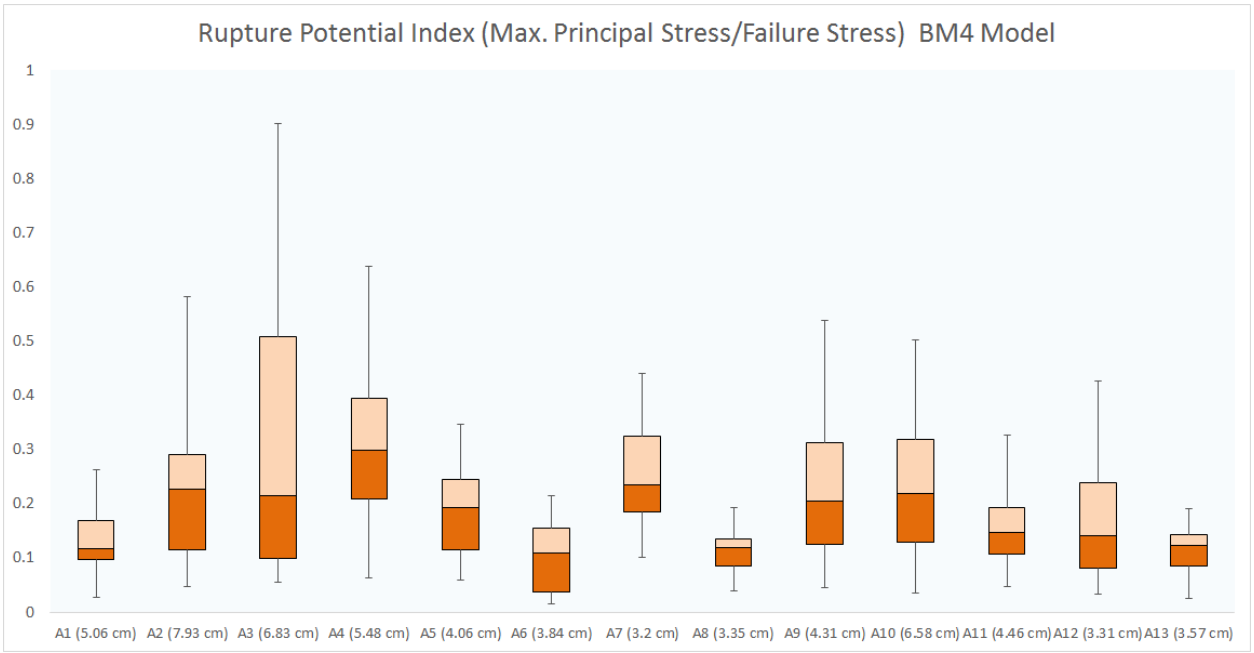

Figure 32: Rupture Potential Index for strength of the BM4 Material Model.

Comparisons of Various Indices for Ruptured and Unruptured AAA (BM4 Model)

Statistics were performed to test whether or not ruptured aneurysms had higher wall pressure induced wall tension than unruptured aneurysms using the Mann-Whitney non-parametric statistical test. Additional indices such as pressure induced wall stress, RPI tension and RPI stress were also compared. These results are tabulated in Table 4 of the p-values comparing various indices of ruptured and unruptured aneurysms. Figure 33 – 34 display the peak wall tension (95th percentile) of pressure induced wall tension, pressure induced wall stress, RPI tension and RPI stress.

Table 4: Mann-Whitney test p-values of various indices.

	p-value Tension	p-value Stress	p-value RPI-T	p-value RPI-S
BM4	0.053	0.099	0.038	0.038

Figure 33: Peak wall tension and stress comparison between ruptured and unruptured AAA.

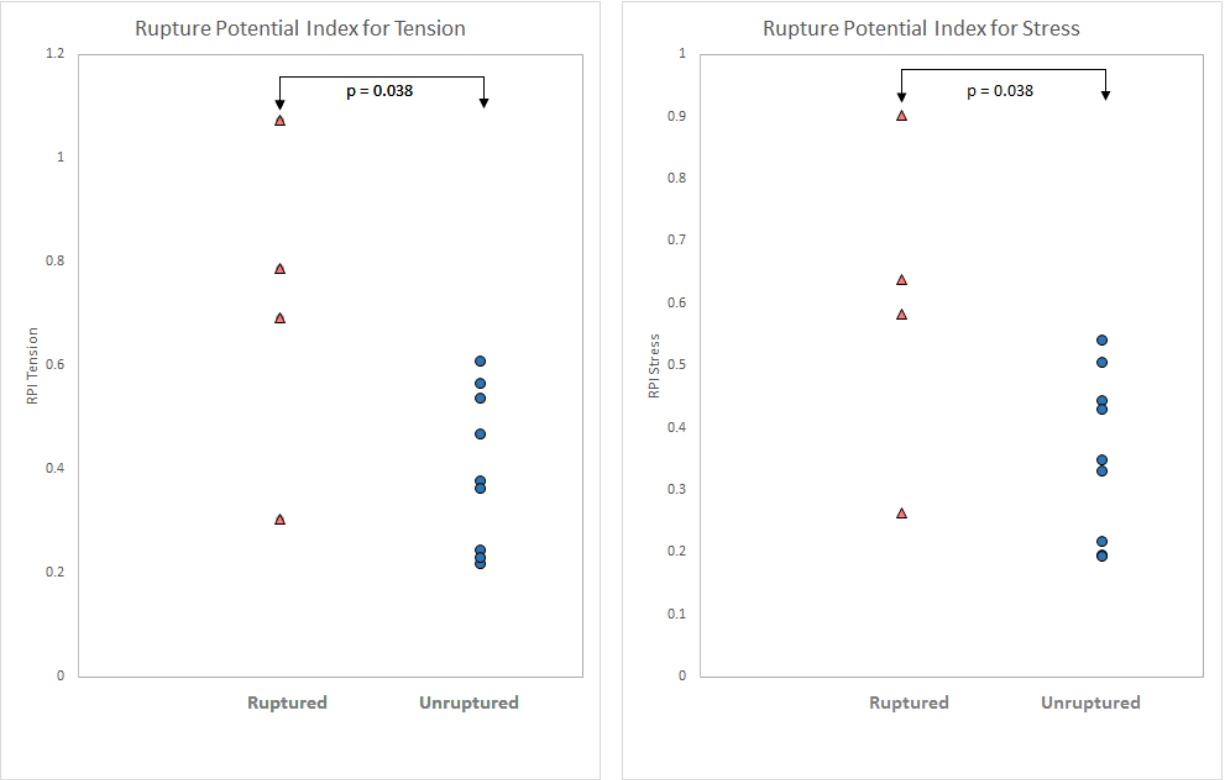

Figure 34: Peak Rupture Potential Index tension and stress comparisons between ruptured and unruptured AAA.

Results for a Representative Noninvasive Finite Element Model (AM3)

Indices that are presented for the AM3 model include wall tension, maximum principal stress, RPI tension and RPI stress. The AM3 is a less complex material model compared to the BM4 model and is defined with the same wall thickness and a single hyperelastic material (one α and β assigned). It is also important to note these material model parameters of uniform thickness and homogeneous material properties allows for model to be constructed noninvasively. Each plot also includes a table of the minimum index value (5^{th} percentile), median and maximum value (95^{th} percentile) and the format is similar to the results presented for the BM4 model.

Figure 35 correspond to the pressure induced wall tension of all aneurysms that were analyzed for the AM3 material model.

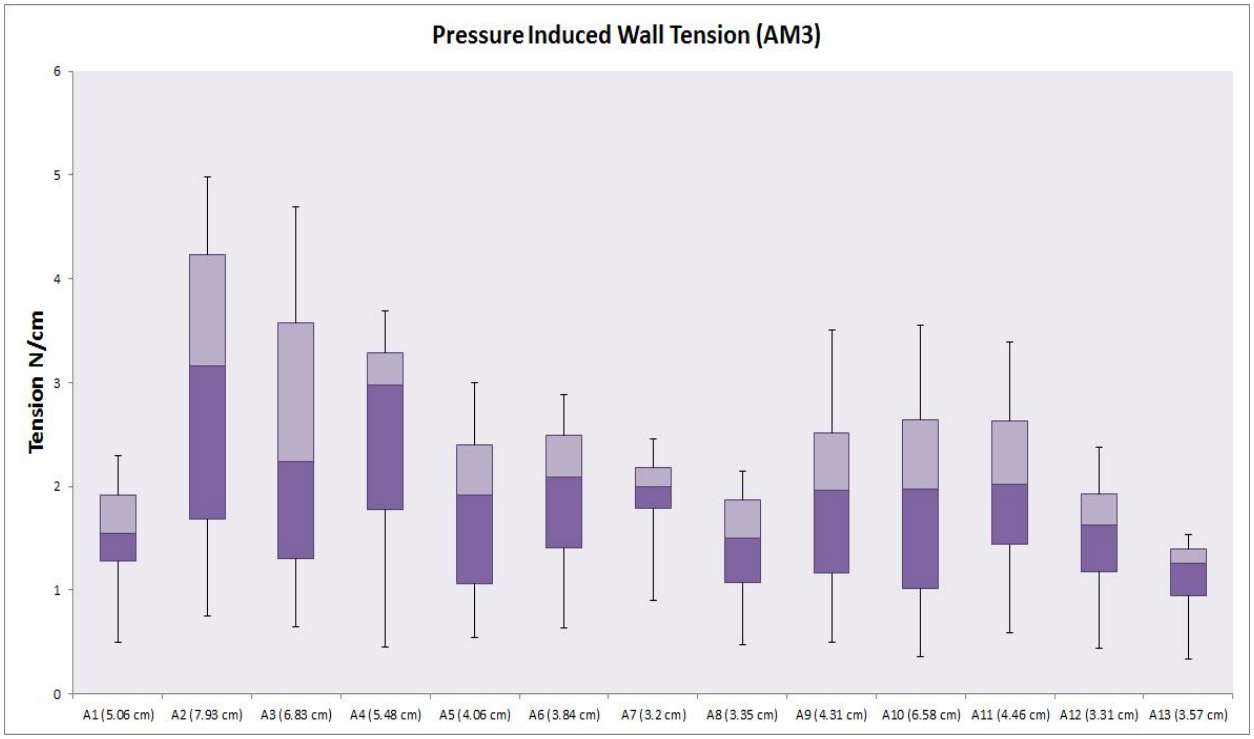

Figure 35*: Pressure induced wall tension box plot of all aneurysms with uniform thickness and single hyperelastic material model.*

Figure 36 correspond to the pressure induced wall stress of all aneurysms that were analyzed for the AM3 material model. Figures 37 – 38 are the RPI tension and RPI stress for the AM3 material model.

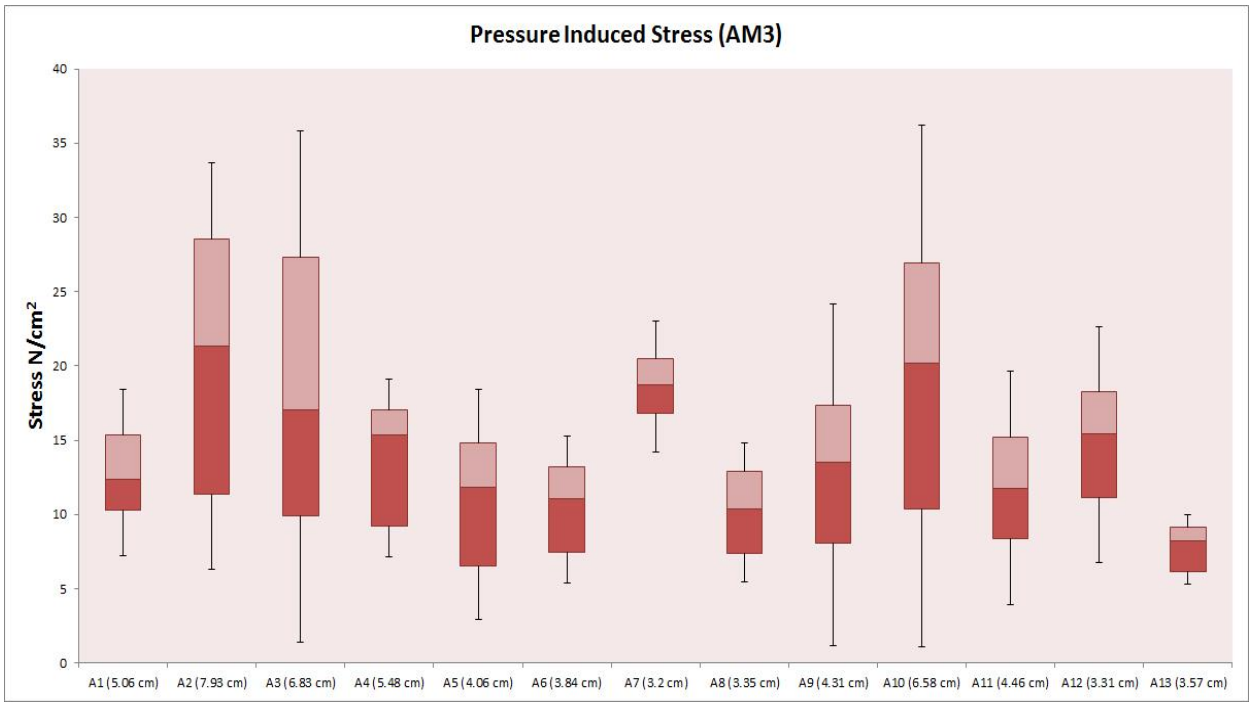

Figure 36: *Pressure induced maximum principal stresses boxplot of the AM3 model for all aneurysms.*

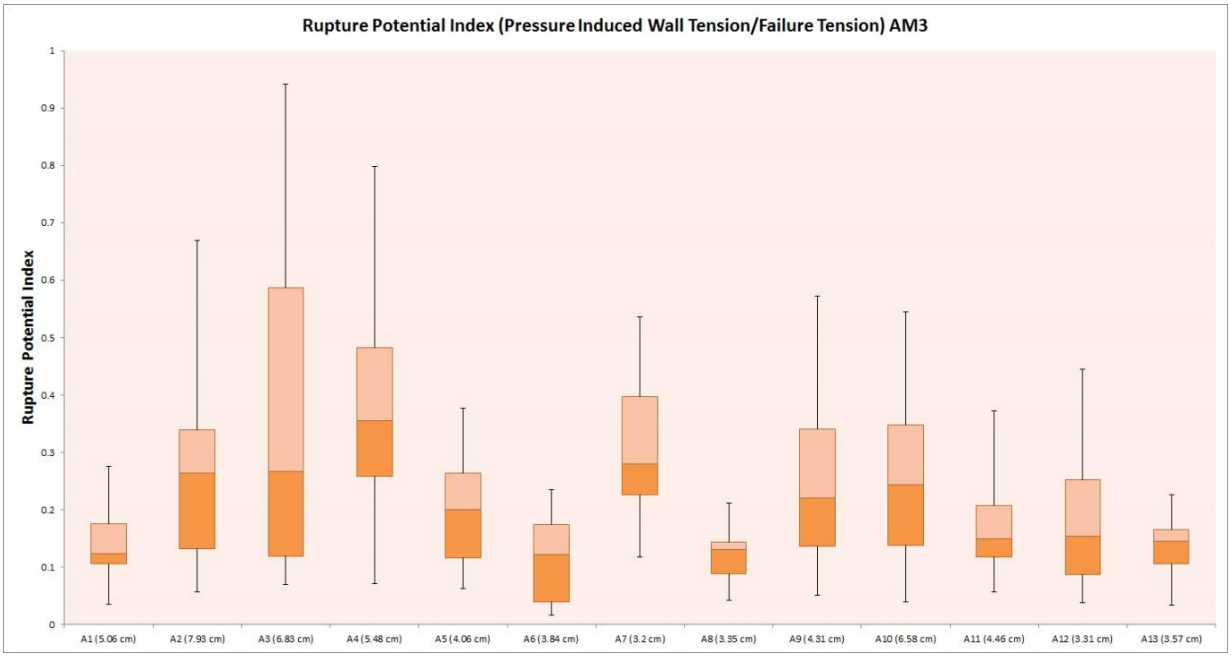

Figure 38: Rupture Potential Index for tension of the AM3 model.

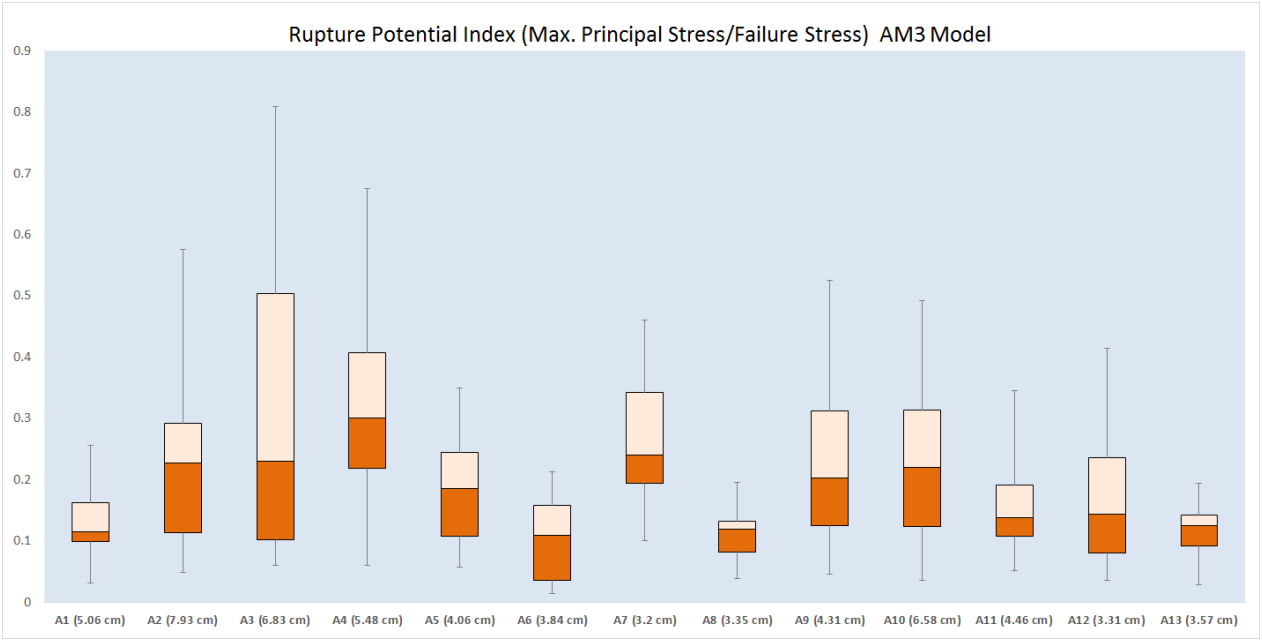

Figure 37: Ruture Potential Index for stress of the AM3 model.

Results for All Models: Ruptured vs. Unruptured Aneurysms

Statistics for the BM4 model were presented in Table 4 earlier, Table5 displays p-values from the Mann-Whitney test for all material models and will be discussed in further detail.

Table 5: Mann-Whitney test p-values of various indices for all models

	p-value Tension	p-value Stress	p-value RPI-T	p-value RPI-S
AM3	0.0531	0.207	0.0378	0.0378
BM4	0.0531	0.0993	0.0378	0.0378

Comparisons of the AM3 and BM4 Material Models

Figure 39 displays the tension of both the AM3 and BM4 models side by side in the anterior and posterior views. The AM3 tension plot is generally much smoother than the BM4 tension plot because of the uniform thickness and homogeneous material properties. There are very little differences between the tension plots for uniform thickness and variable wall thickness and this will be discussed in the later section.

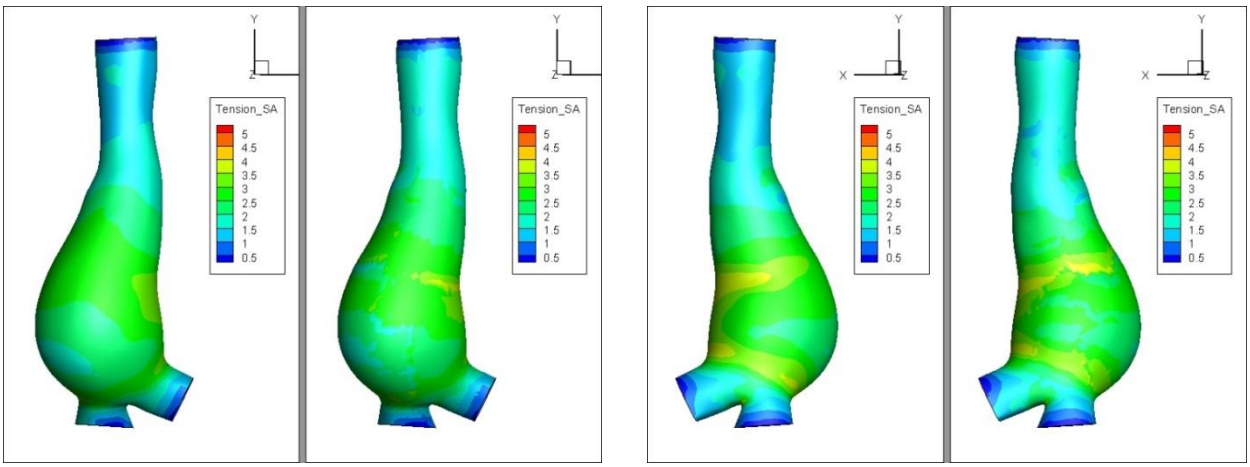

Figure 39: *Anterior view of AM3 vs. BM4 tension plot (left) and Posterior view of AM3 vs. BM4 Tension plot (Right).*

The RPI Tension is displayed with both the AM3 and BM4 models in the anterior and posterior views (Figure 40). RPI Tension was derived from the known failure tension on the mesh surface to the calculated tension on the surface using Equation 7 [23]. Figure 40 is representative of the pressure induced wall tension found in Figure 37 divided by the experimentally determined and interpolated wall failure tension found in Figure 28. Similarly Figure 41 is the RPI stress derived from dividing the pressure induced wall stress by the wall failure strength found in Figure 28.

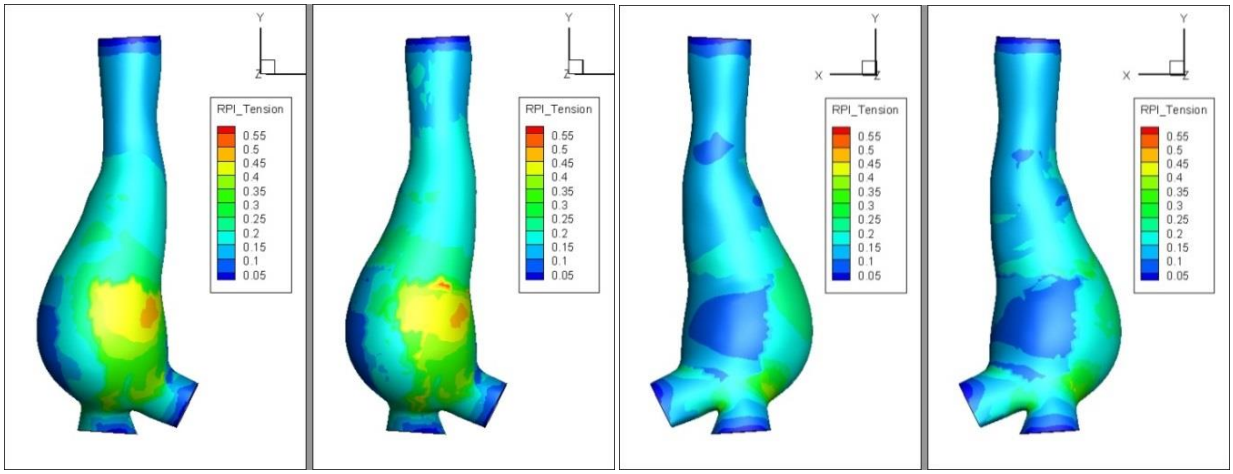

Figure 40: *Anterior view of AM3 vs. BM4 RPI Tension (left) and Posterior view of AM3 vs. BM4 RPI Tension (Right).*

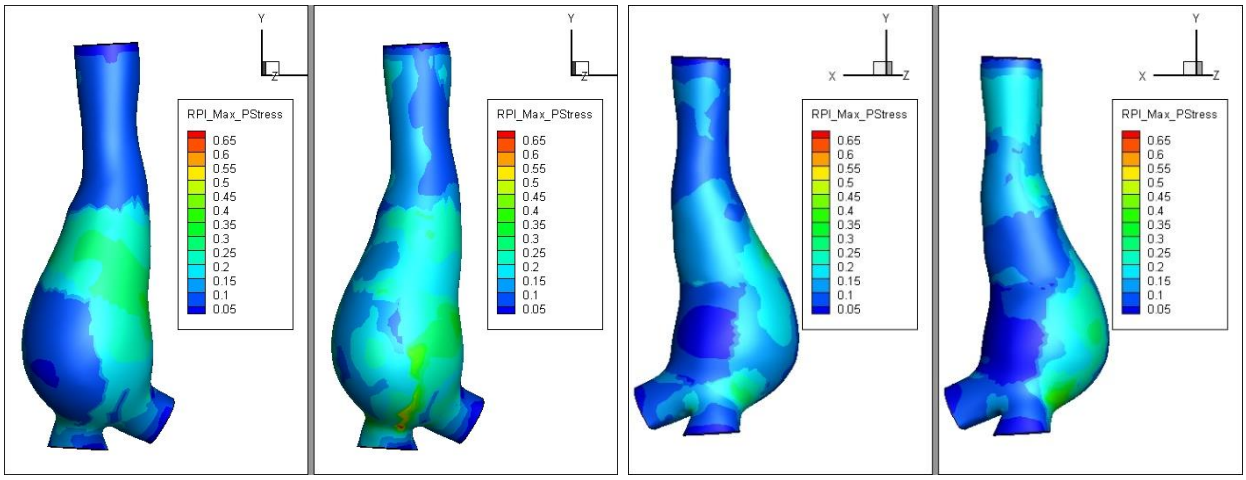

Figure 41: *Anterior view of AM3 vs. BM4 RPI Stress (left) and Posterior view of AM3 vs. BM4 RPI Stress (Right).*

Tables 6 – 9 compare pressure induced wall tension, pressure induced wall stress, RPI tension and RPI stress of the material models AM3 and BM4 side by side for quick comparisons. Pressure induced wall stress has the largest variance of all indices

Table 6: Pressure induced wall tension min (5th percentile), median, max (95th percentile) of models AM3 and BM4.

	A1	A2	A3	A4	A5	A6	A7	A8	A9	A10	A11	A12	A13
AM3 5th	0.50	0.75	0.65	0.45	0.55	0.64	0.90	0.47	0.50	0.35	0.59	0.43	0.34
BM4 5th	0.45	0.69	0.56	0.50	0.52	0.61	0.89	0.49	0.45	0.36	0.52	0.37	0.30
AM3 50th	1.54	3.16	2.24	2.97	1.92	2.09	2.00	1.50	1.96	1.98	2.02	1.62	1.26
BM4 50th	1.59	3.22	2.37	2.83	2.00	2.04	1.95	1.53	1.96	2.00	2.03	1.63	1.22
AM3 95th	2.30	4.99	4.69	3.69	2.99	2.88	2.46	2.14	3.50	3.55	3.38	2.38	1.53
BM4 95th	2.34	4.97	4.77	3.77	3.07	3.01	2.40	2.16	3.55	3.60	3.28	2.46	1.59

Table 7: Pressure induced maximum principal stress (N/cm2) minimum (5th percentile), median, and maximum (95th percentile) for AM3 and BM4 models.

	A1	A2	A3	A4	A5	A6	A7	A8	A9	A10	A11	A12	A13
AM3 5th	4.01	5.05	4.96	2.35	3.36	3.39	8.47	3.27	3.42	3.61	3.41	4.13	2.19
BM4 5th	4.09	4.15	4.33	2.16	3.54	3.35	9.08	3.06	3.65	3.81	3.44	3.82	1.46
AM3 50th	12.38	21.32	17.05	15.38	11.82	11.04	18.74	10.35	13.54	20.16	11.71	15.41	8.21
BM4 50th	15.00	22.48	18.38	14.49	12.73	10.32	18.35	10.01	15.49	19.51	12.98	16.43	8.12
AM3 95th	18.42	33.65	35.79	19.09	18.42	15.25	23.03	14.80	24.16	36.19	19.64	22.60	10.00
BM4 95th	29.39	40.70	42.88	30.28	24.26	21.26	33.34	17.83	60.05	41.59	28.99	26.62	14.88

Table 8: RPI tension min (5th percentile), median, max (95th percentile) of models AM3 and BM4.

	A1	A2	A3	A4	A5	A6	A7	A8	A9	A10	A11	A12	A13
AM3 5th	0.034	0.057	0.070	0.070	0.062	0.016	0.118	0.043	0.050	0.039	0.056	0.038	0.033
BM4 5th	0.033	0.055	0.065	0.077	0.064	0.017	0.123	0.044	0.050	0.040	0.053	0.036	0.031
AM3 50th	0.123	0.264	0.267	0.355	0.200	0.121	0.279	0.130	0.221	0.244	0.149	0.153	0.145
BM4 50th	0.136	0.271	0.256	0.368	0.208	0.122	0.285	0.133	0.231	0.245	0.162	0.153	0.147
AM3 95th	0.275	0.669	0.941	0.798	0.377	0.234	0.536	0.212	0.573	0.545	0.373	0.444	0.226
BM4 95th	0.305	0.693	1.073	0.788	0.375	0.242	0.536	0.215	0.606	0.563	0.362	0.465	0.227

Table 39: RPI stress min (5th percentile), median, max (95th percentile) of models AM3 and BM4.

	A1	A2	A3	A4	A5	A6	A7	A8	A9	A10	A11	A12	A13
AM3 5th	0.032	0.049	0.060	0.060	0.058	0.015	0.101	0.039	0.046	0.035	0.052	0.036	0.028
BM4 5th	0.028	0.046	0.055	0.062	0.059	0.015	0.101	0.040	0.044	0.035	0.048	0.033	0.026
AM3 50th	0.114	0.227	0.230	0.300	0.185	0.110	0.240	0.120	0.202	0.221	0.138	0.143	0.124
BM4 50th	0.118	0.227	0.215	0.298	0.193	0.108	0.234	0.120	0.205	0.218	0.147	0.140	0.123
AM3 95th	0.256	0.576	0.809	0.676	0.349	0.212	0.460	0.195	0.526	0.492	0.345	0.415	0.194
BM4 95th	0.263	0.582	0.902	0.638	0.347	0.215	0.441	0.194	0.539	0.503	0.328	0.428	0.191

CHAPTER 4: DISCUSSION

In the current study, computational finite element modeling that accommodates patient-specific geometries and regional heterogeneities in various wall properties based on experimental data was performed. The results were used to test the hypothesis:

Pressure induced wall tension in ruptured aneurysms is higher than that in unruptured aneurysms.

It has been suggested that the aneurysm wall of ruptured aneurysms are not weaker on average than unruptured aneurysms in a previous study [4]. The current study compares the pressure induced artery wall tension and stress between four ruptured aneurysms and nine unruptured aneurysms.

Interpolation Effects on the Computational Models

A method for interpolating scalar values on the mesh surface was used to fill in the gaps of unknown scalar values on the mesh surface of each aneurysm. Measured thicknesses and material properties (alpha, beta coefficients, failure stress, and failure tension) were used in the development of the all parameter model (BM4) and for post-processing calculations. The results of the thickness interpolation and coefficient weighting were found to be suitable as the method was able to retain original thickness values at a known point on the surface. Out of all of the experimental data that was collected, the thickness information had the greatest density of measurement for each aneurysm in the anterior, posterior, left and right faces of the aneurysms.

The lack of material properties data was the weak link in implementing the interpolation and weighted coefficient method in the development of the all parameter finite element model. The low density of valid material properties data affects the values of wall properties, tension calculations, and RPI calculations. For instance, Aneurysm 13 had a total of eight specimens tested with only three valid uniaxial extension tests (validity determined by not having any slipping or tearing at the clamps). The three valid material properties were interpolated on the mesh surface cannot give an accurate account of the actual material properties at each location on the mesh surface. This in turn affects the calculations of the Rupture Potential Index while incorporating the failure stress and failure tension properties (Equation 7).

It could also be stated the interpolation of thicknesses may not be sufficient to capture all of the unknown points on the aneurysm mesh surface. There is a relatively low density of known thickness nodes in comparison to the number of nodes in the entire mesh surface of each aneurysm model. The manner in which the unknown thicknesses are calculated do not allow for the thickness at any point to exceed the maximum known thickness or dip below the minimum known thickness in a given aneurysm data set. The known thicknesses are poles that the unknown thicknesses are weighted with and it is a poor assumption that the thicknesses would not exceed or dip below the known maximum and minimum measured aneurysm wall thicknesses. The thicknesses have a direct effect on how the pressure induced maximum principal stress is calculated.

Tension vs. Stress in the Computational Models

Figures 24-26 represent summaries of each aneurysm with experimental data collected (thicknesses, failure stress and failure tension). Ruptured aneurysm's (A1 through A4) experimental values (thicknesses or failure properties) are within the range of the unruptured aneurysms. Viewing the measured data as a whole, there are no perceivable differences between the measured thicknesses and failure properties between ruptured and unruptured aneurysms as reported earlier by Raghavan et al. [4]

The failure properties are derived from the load-displacement data that is extracted from uniaxial extension tests (Equations 1a, 1b). The failure stress in each specimen represents the maximum stress through the thickness, whereas the failure tension is representative of the maximum tension of the tissue while removing the thickness information. The differences between the failure tension plots and failure stress plots are evident as the thicknesses drive the characteristics of each respective index (Figures 25-26). The failure tension embodies the geometrical contribution of the tissue while the failure stress incorporates the wall characteristics with inclusive thickness.

The purpose of the finite element modeling was to retrieve pressure induced wall tension and wall stress. Researchers have generally reported finite element analysis results as stress rather than tension [4, 5, 10, 11, 16-19, 22, 23, 26] . Stress does not capture the pure geometrical contribution of the driving pressure load as it includes the relatively unknown stress across the thickness. Pressure induced stress calculations are heavily dependent on the average thickness of each element (average of the nodes that define the element). The maximum pressure induced principal stress for the uniform thickness model and the variable

thickness model differ in the magnitude and location of the maximum stress due to the variations in thickness.

The uniform thickness models that present stress are in reality presenting wall tension at a different magnitude across the defined uniform thickness (the direction normal to the surface). Figures 35 and 29 of the AM3 tension plot and BM4 tension plot reiterate this point clearly as there is very little difference between the derived tension with uniform thickness or variable thickness. Figure 36 the uniform thickness, uniform material properties model (AM3) share the same overall shape (at a different magnitude) with the AM3 and BM4 tension plots found in Figures 35 and 29. Figure 42 shows that these two tension plots are positively correlated with an R^2 value close to 1 with the maximum tension values in the same region (see Figure 40).

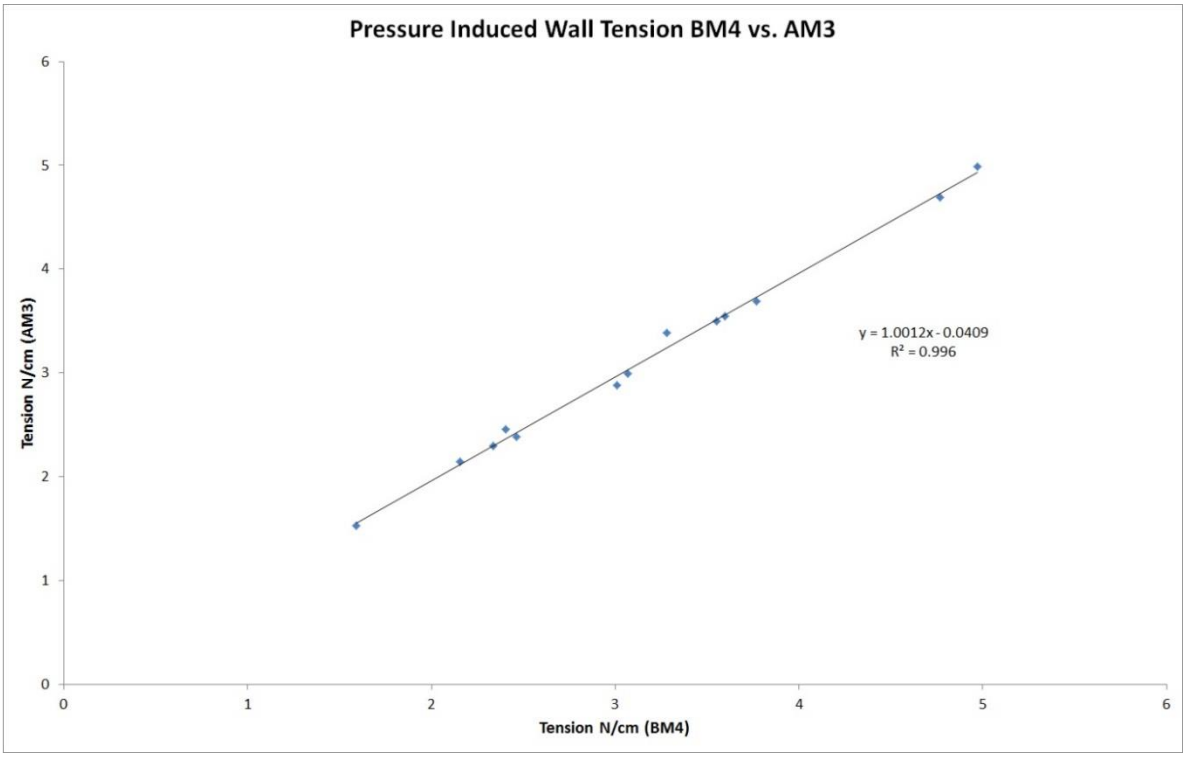

Figure 42: *Pressure induced wall tension BM4 vs. AM3 comparison plot.*

Reporting results as tension rather than stress alleviates the need to know the thickness of the wall at each location. Trying to predict wall thicknesses, implementing methods to estimate thickness and making physical measurements of aneurysm wall thickness may not be as necessary as once thought. Pressure induced wall stress does not isolate where across the thickness of the aneurysm wall the maximum stress is occurring and tension does not require thickness information. The location of the maximum pressure induced stress would correspond to the thinnest region of the aneurysm whereas the location of the maximum pressure induced tension would correspond to the maximum tension the aneurysm is subjected to (but not necessarily the weakest spot).

Orientation of the Maximum Principal Stress and Tension

Tension is derived by the principal directions of stress, specifically the maximum principal stress on the face of each finite element (shell elements). The minor principal axis was generally defined in the longitudinal direction while the major principal axis of stress is in the circumferential direction. Figure 43 displays the principal axes with the length corresponding to the magnitude. Irrespective of the size and orientation of the triangular shell elements, the principal directions are in agreement with each other. Tension calculations used the maximum principal stress values in the circumferential direction and were multiplied by a volumetric factor of change (thickness multiplied by surface area change).

Orientation of the principal stresses and tension in the longitudinal and circumferential directions suggest that rupture does not occur in random directions. It was observed earlier [4, 16] that the site of rupture followed a geodesic straight line path in the longitudinal direction or perpendicular to the maximum stress/tension on the aneurysm wall in the circumferential

direction. The longitudinal rupture site occurred in a straight line and did not have any jagged edges. This observation supports the notion that the aneurysm wall did not deteriorate completely and that the wall may have failed because of the pressure induced load.

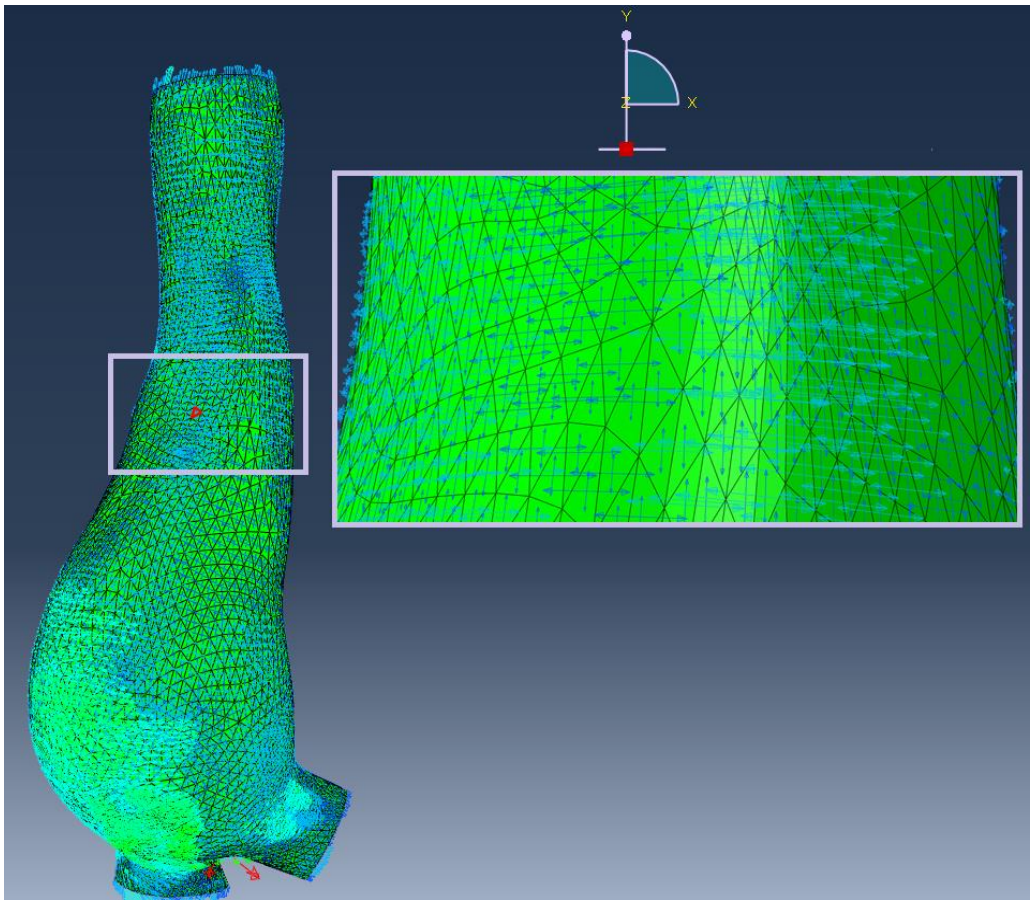

Figure 43: *Abaqus view of the major and minor principal stress axes on the aneurysm mesh surface geometry.*

Rupture Site Predictability, Indices and Computational Modeling

The current study is unique because the material properties and rupture site are known for four post-mortem aneurysms. This section discusses both stress and tension and their respective rupture potential index as predictors of where rupture may occur. These indices have traditionally been used as potential indicators for rupture [18]. Figure 44 presents

multiple views of A2 with its material definitions in the anterior view. Figure 45 displays where the aneurysm actually ruptured in the 'left' view of A2.

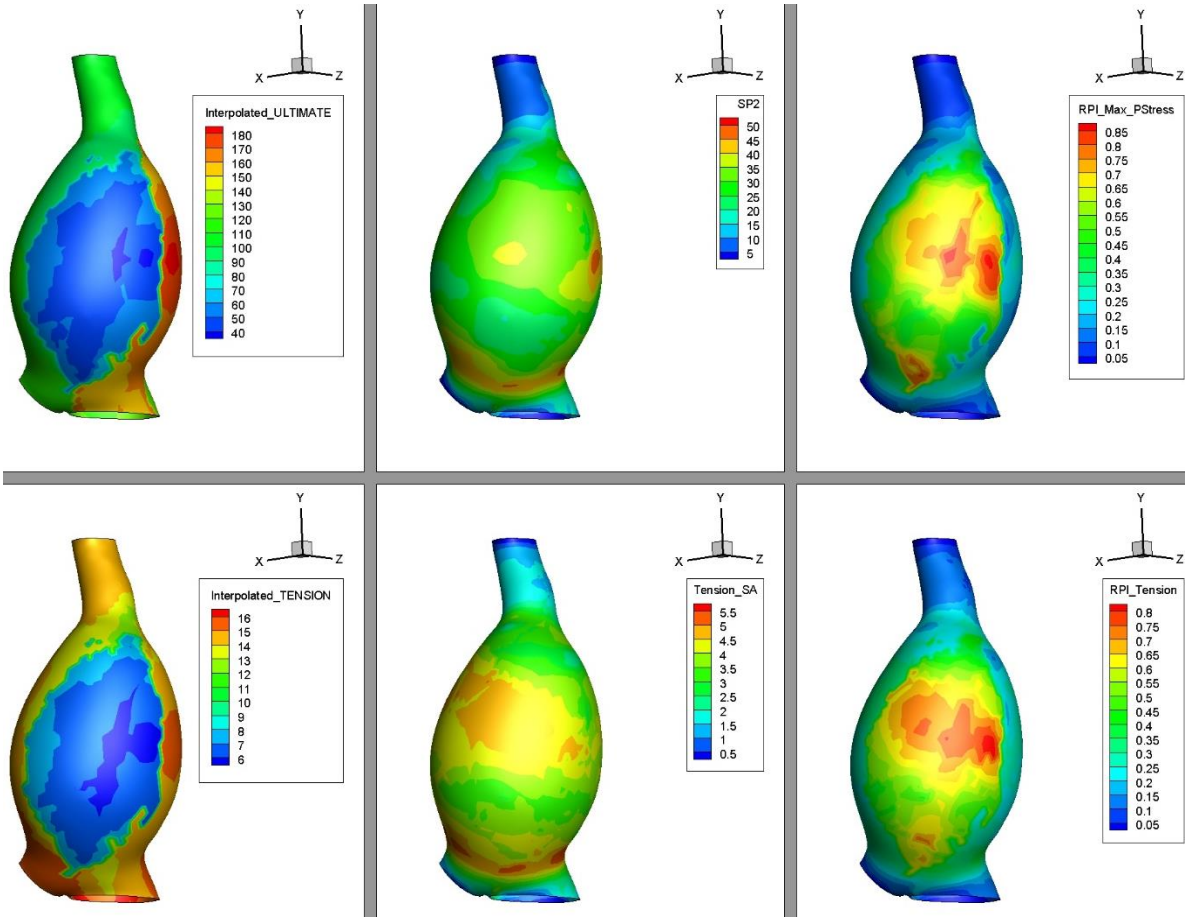

Figure 44: *Aneurysm 2 BM4 Model Top Row: (left to right) Interpolated Failure Stress, Maximum Pressure Induced Wall Stress (SP2) and RPI Stress. Bottom Row: Interpolated Failure Tension, Pressure induced wall tension and RPI Tension.*

If strictly observing the pressure induced maximum principal stress and the maximum tension it would be unlikely that the location of rupture would be known. It is seen that the maximum pressure induced principal stress and tension occur in the lower posterior region instead of where the actual rupture is located on the left side of A2. The interpolated failure tension and interpolated failure stresses are seen in Figure 44. As the radius of curvature

increases to the maximum diameter, the wall failure properties decrease in strength for A2 and its failure properties. The RPI Tension and RPI Stress essentially report similar values because it is a percentage of the maximum pressure induced stress and tension with the experimental failure stress and failure tension (i.e. removing thickness effects on the model).

The difficulty with prediction of rupture is that the maximum pressure induced stress and maximum pressure induced tension do not always correspond to where the weakest point of the aneurysm is. The plots that are shown only display where the maximum pressure induced wall tension or wall stress is located. The RPI captures where the highest potential of rupture may occur in an aneurysm based on the known failure properties that were interpolated. The location of the maximum RPI was roughly located at the top or proximal end of the longitudinal tear of the aneurysm. The pressure induced tension that corresponds to the maximum RPI is in the 90th percentile of the pressure induced tension of the aneurysm. The 90th percentile tension, RPI tension and RPI stress are in agreement.

Figure 45: *Left view of A2 rupture site.*

The RPI tension and RPI stress report values that are similar because of the way that each index is calculated. The rupture potential index for stress is essentially reporting the same information as the rupture potential index for tension. The pressure induced wall stress is derived from the thickness information and the failure stress is also calculated using the thickness information. The RPI is a dimensionless index as it divides the pressure induced values by the failure properties in the same unit of measurement. Any contribution the thickness had on the stress was removed when dividing by the failure stress properties that include thickness information as well.

Ruptured aneurysms A1, A3 and A4 along with their rupture sites are found in Appendix I. Aneurysm 1 ruptured in the lower left posterior region of the aneurysm, aneurysm 3 ruptured in the upper left region and aneurysm 4 ruptured in the central right region. The maximum principal stress is located in the dilated region where the rupture took place whereas the tension in the rupture location was about the 85^{th} percentile of pressure induced tension.

Aneurysm 3 in the right view seems to have a stress or tension concentration located in mid-upper right view of the aneurysm where the highest maximum principal stress and maximum RPI stress is located. The maximum RPI tension is also located in the right region. However, the location of the rupture occurred in the left view. The maximum pressure induced wall tension occurred in the left region but at a geometric concavity rather than the aneurysm body. Aneurysm 4 does not have any agreement on where rupture occurred and the maximum pressure induced wall stress and tension. The largest pressure induced stress and tension occurs in the right region of the aneurysm at a concavity and the highest RPI occurs in the posterior region.

The given indices; maximum pressure induced stress, max pressure induced wall tension and max RPI do not coincide with the location of the rupture site except for A2. The main purpose of the current study was not to test the validity of these indices, but rather investigate the differences of these values between ruptured and unruptured aneurysms. It would be have been encouraging to see the maximum values match the rupture site, but there were limitations to the post-processing of the computational results.

The post-processing for the RPI lacks a high density of material property points that are used to divide the computational results (pressure induced stress and tension). The lack of density of material properties hinders that ability for the RPI to be reliable in this study. The consequence of having a low density of wall failure properties is that the RPI could be misrepresented based on the known wall failure properties that were interpolated. It was previously mentioned that stress is related to the thickness of the arterial wall and that the tension found from the AM3 model (uniform thickness and homogenous material properties) and BM4 model (variable wall thickness and variable material properties) had a high correlation of maximum tension in the aneurysm. The modeling choice (material properties and thicknesses) and available data may not be as significant as once thought when performing the finite element analysis for pressure induced wall tension.

Do Ruptured Aneurysms Have Higher Pressure Induced Wall Tension?

The previous sections have led to the discussion of the hypothesis on whether or not ruptured aneurysms undergo higher pressure induced wall tension that unruptured aneurysms. A statistical approach using the Mann-Whitney test resulted in Table 5 in the results section. With a statistical significance set at $p < 0.05$, it is fair to say that the peak wall tension is not

higher in ruptured AAA with statistical significance ($p = 0.053$). However, with a $p = 0.053$, there is a trend toward ruptured aneurysms having a higher peak wall tension than unruptured aneurysms. The rupture potential index for tension and stress can be stated as having a higher rupture potential in ruptured aneurysms than unruptured aneurysms. The p-value for stress was found to be not statistically significant for both the AM3 model and BM4 model.

There are obvious limitations to the statistical approach taken to test the aneurysm population. A non-parametric test was used because of the low population size and the probability that the ruptured aneurysm group and unruptured group were not normally distributed. Due to the nature of the aneurysm data being available, there was no possibility of determining statistical power prior to the study being conducted. With the given limitations stated it could be entirely possible that with a higher aneurysm population, the p-value could increase or decrease for the tension index (initial hypothesis). The RPI tension p-value can also give a false sense of security as the RPI tension was derived by the scarce material properties data that was interpolated (previous limitation stated earlier).

Conclusion

The current study and its methods include one of the first computational models with heterogeneous material properties and variable wall thicknesses that were measured post-mortem. The goal was to test whether or not ruptured aneurysms were subject to a higher pressure induced wall tension than unruptured aneurysms. Results are not consistent with the hypothesis that ruptured aneurysms have higher peak wall tension than unruptured aneurysms. But a Mann Whitney U test p-value of 0.053 suggests a trend toward consistency with the hypothesis and so this remains to be evaluated with larger study populations.

Observations were also made on the implementation of the computational models as well as the analysis of the results that were tabulated after each computational model was calculated. It was shown that uniform thickness with a single hyperelastic material model that has been seen in literature have really been reporting the tension the aneurysm is under (only at a different magnitude). The pressure induced tension models that were presented for uniform thickness and a single hyperelastic material model and the variable thickness heterogeneous material model were seen to be corollary. The presentation of the computational model choices and the case for pressure induced wall tension in this body of work may alleviate the need to know the measured values (wall thickness and material properties) for others performing computational abdominal aortic aneurysm research.

It was also noted that the Rupture Potential Index or the percentage of pressure induced strength and failure strength is really presenting the rupture potential index for tension as the thicknesses information has been removed (as thickness information is embedded in the derivation of stress). Failure strength properties for the RPI have traditionally used a stochastic model to estimate the failure strength at different locations on an aneurysm, and this study used actual failure strength data that was interpolated on the entire aneurysm surface. The major limitation of the latter method was the low density of failure properties measurements for each aneurysm. However, deriving the failure strength from the load displacement data serves as a reminder that the failure strength properties include thickness information (something that may have been overlooked in calculating failure strength from a stochastic equation).

In the future studies, a higher population of ruptured aneurysms and unruptured aneurysms may shed light on whether or not rupture is primarily caused by an elevation of pressure induced wall tension. For all practical purposes, the ruptured aneurysms that were

compared with the unruptured aneurysms had a greater maximum diameter. It would be expected that the ruptured aneurysms group would have had a higher pressure induced tension than the unruptured group. It is hopeful that ruptured aneurysms with diameters less than the maximum diameter criteria be found to perform similar computational tests to help clinicians determine ruptured risk of aneurysms of all sizes.

APPENDIX: RUPTURED ANEURYSM PLOTS AND RUPTURE LOCATIONS

Aneurysm 1 Posterior View only

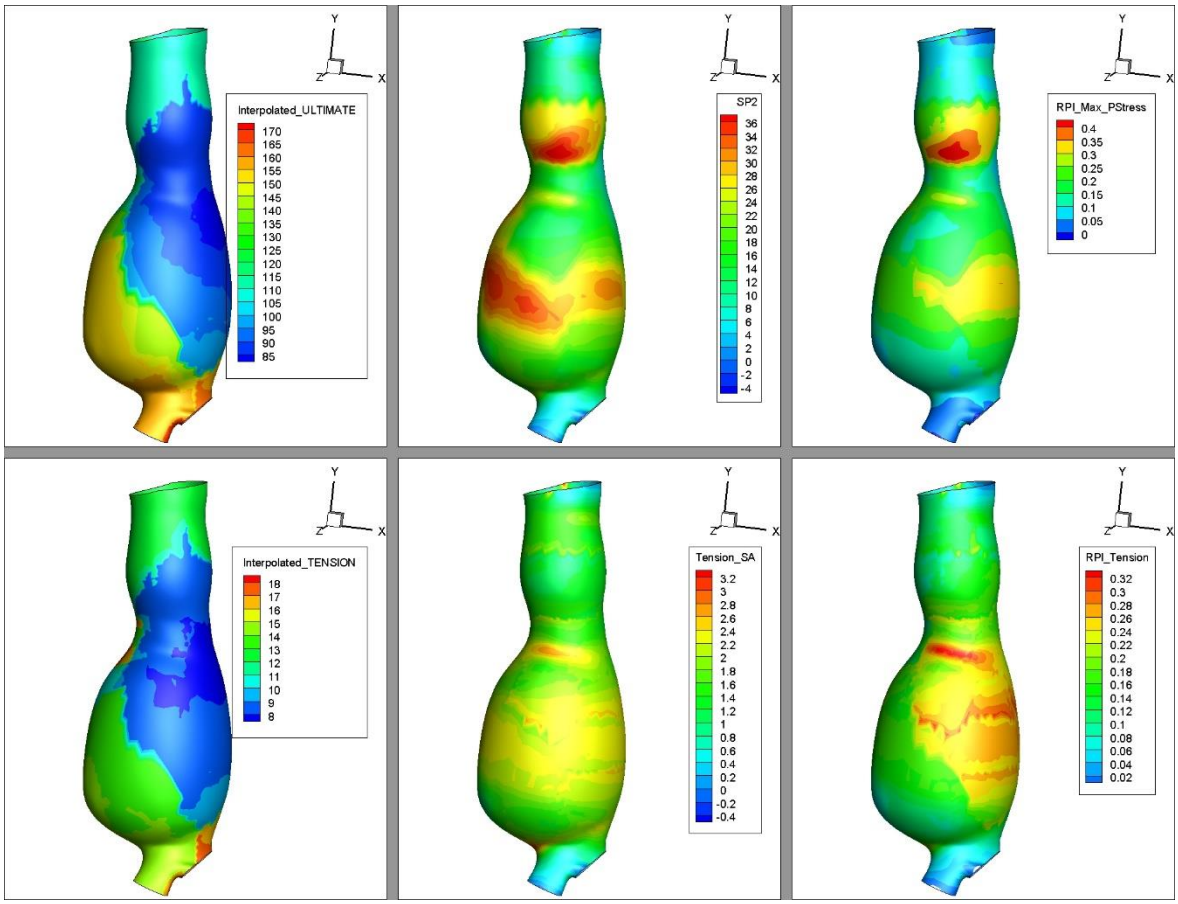

Aneurysm 3: Left and Right Views

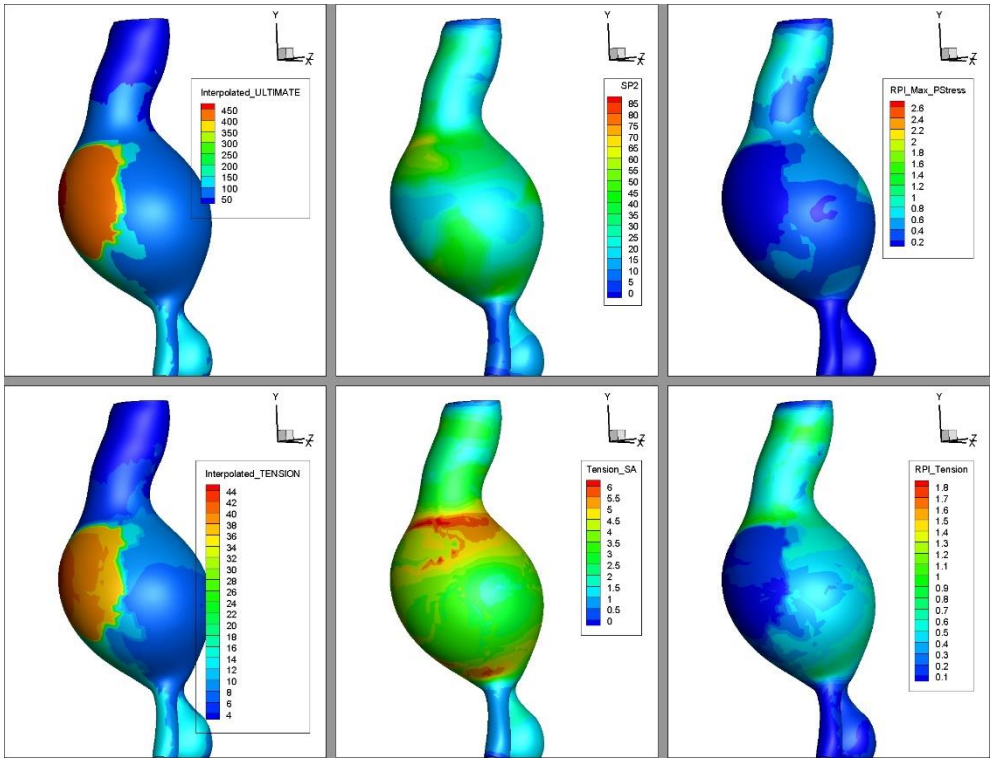

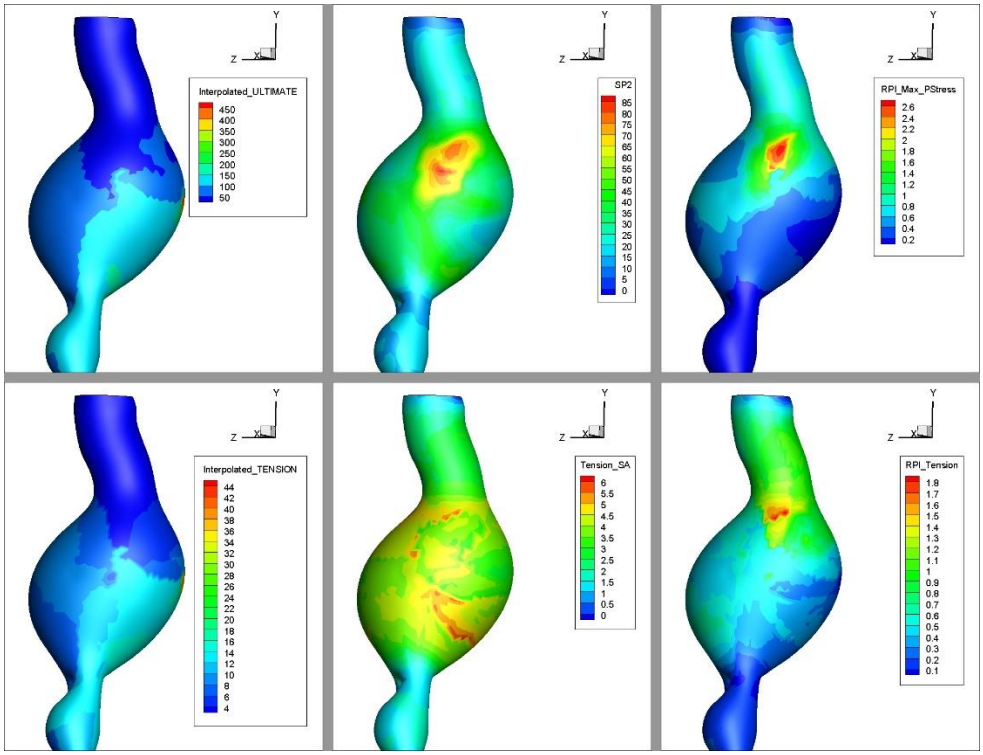

Aneurysm 4 Left and Right Views

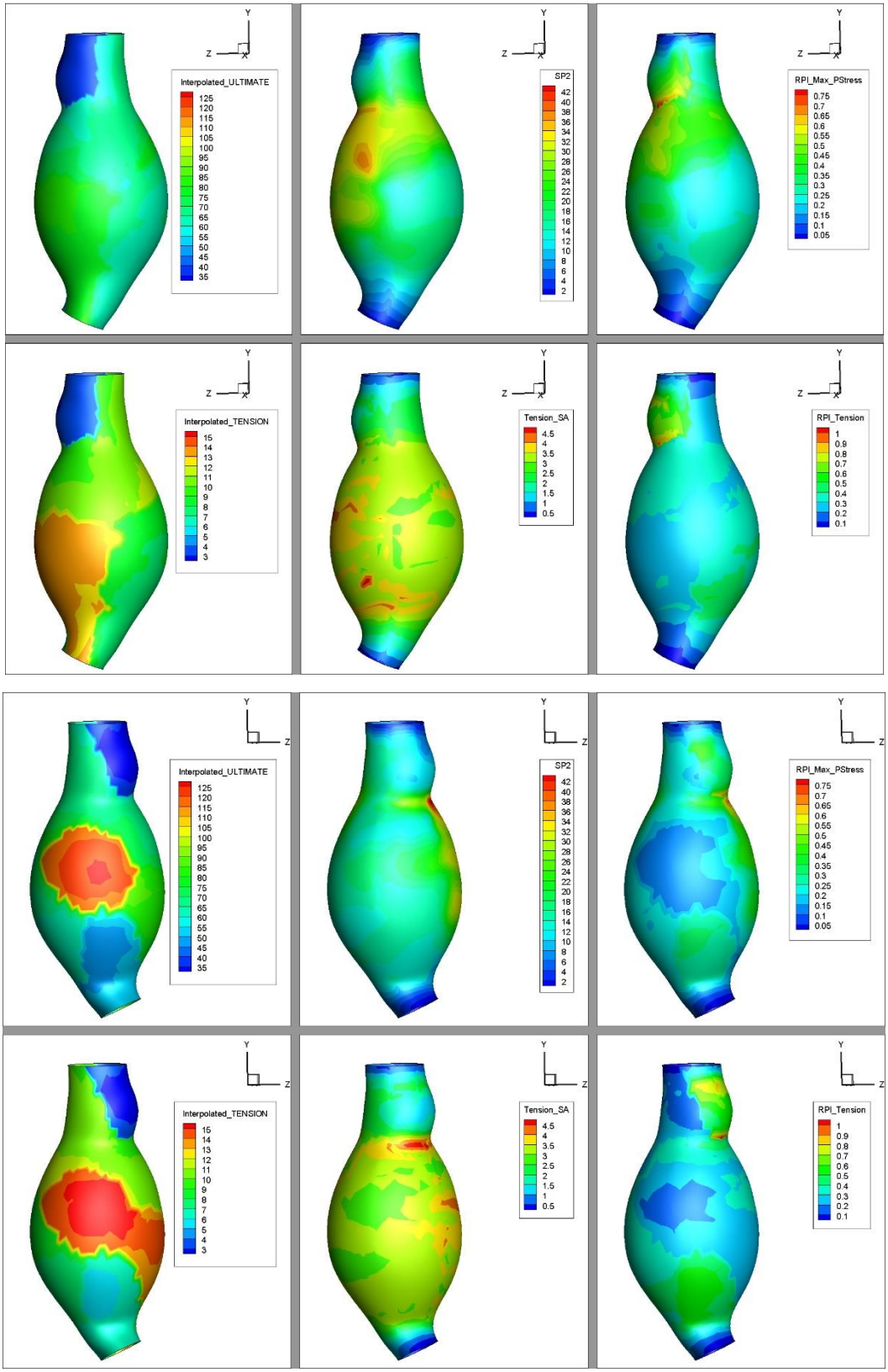

Aneurysm 1, 3 and 4 Rupture Site Locations

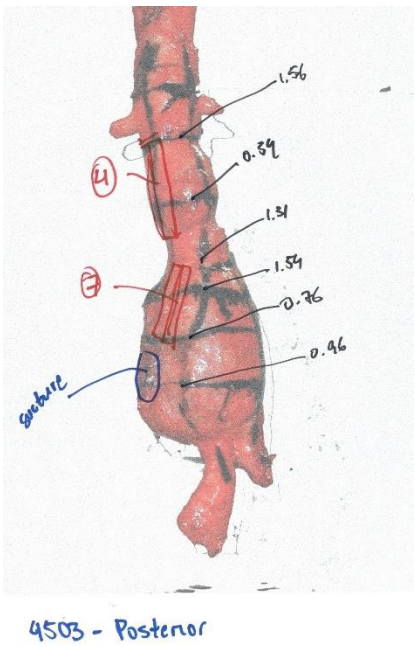

Aneurysm 1: Posterior Rupture

Aneurysm 3: Left Rupture

Aneurysm 4: Right Rupture

REFERENCES

1. Darling, R.C., et al., *Autopsy study of unoperated abdominal aortic aneurysms. The case for early resection.* Circulation, 1977. 56(3 Suppl): p. II161-4.

2. Group, O.S.P.U.o.P.a.D.-C., *MeshLab*, 2005 - Current, SourceForge.net: Italy. p. 3D model viewer and mesh editor

3. McNeel, *Rhinoceros 3D Nurbs Modeler*, 2011: Seattle, WA. p. Modeling tools for designers.

4. Raghavan, M.L., et al., *Biomechanical failure properties and microstructural content of ruptured and unruptured abdominal aortic aneurysms.* Journal of Biomechanics, 2011. 44(13): p. 2501-2507.

5. Vorp, D.A., *Biomechanics of abdominal aortic aneurysm.* Journal of Biomechanics, 2007. 40(9): p. 1887-1902.

6. Bhimji, S., Zieve, David, ADAMs, National Institute of Health. *Abdominal aortic aneurysm*

7. Adam van der Vliet, J. and A.P.M. Boll, *Abdominal aortic aneurysm.* The Lancet, 1997. 349(9055): p. 863-866.

8. Di Martino, E., et al., *Biomechanics of abdominal aortic aneurysm in the presence of endoluminal thrombus: Experimental characterisation and structural static computational analysis.* European Journal of Vascular and Endovascular Surgery, 1998. 15(4): p. 290-299.

9. Doyle, B.J., et al., *On the influence of patient-specific material properties in computational simulations: A case study of a large ruptured abdominal aortic aneurysm.* International Journal for Numerical Methods in Biomedical Engineering, 2013. 29(2): p. 150-164.

10. Fillinger, M.F., et al., *Prediction of rupture risk in abdominal aortic aneurysm during observation: Wall stress versus diameter.* Journal of Vascular Surgery, 2003. 37(4): p. 724-732.

11. Fillinger, M.F., et al., *In vivo analysis of mechanical wall stress and abdominal aortic aneurysm rupture risk.* Journal of Vascular Surgery, 2002. 36(3): p. 589-597.

12. Maier, A., et al., *A Comparison of Diameter, Wall Stress, and Rupture Potential Index for Abdominal Aortic Aneurysm Rupture Risk Prediction.* Annals of Biomedical Engineering, 2010. 38(10): p. 3124-3134.

13. Martufi, G., et al., *Three-Dimensional Geometrical Characterization of Abdominal Aortic Aneurysms: Image-Based Wall Thickness Distribution.* Journal of Biomechanical Engineering, 2009. 131(6): p. 061015-11.

14. Martufi, G.G., Christian T., *Review: The Role of Biomechanical Modeling in the Rupture Risk Assessment for Abdominal Aortic Aneurysms.* Journal of Biomedical Engineering, 2012. 135(2): p. 10.

15. Raghavan, M., M. Webster, and D. Vorp, *Ex vivo biomechanical behavior of abdominal aortic aneurysm: Assessment using a new mathematical model.* Annals of Biomedical Engineering, 1996. 24(5): p. 573-582.

16. Raghavan, M.L., et al., *Regional distribution of wall thickness and failure properties of human abdominal aortic aneurysm.* Journal of Biomechanics, 2006. 39(16): p. 3010-3016.

17. Raghavan, M.L., et al., *Three-dimensional finite element analysis of residual stress in arteries.* Ann Biomed Eng, 2004. 32(2): p. 257-63.

18. Raghavan, M.L. and D.A. Vorp, *Toward a biomechanical tool to evaluate rupture potential of abdominal aortic aneurysm: identification of a finite strain constitutive model and evaluation of its applicability.* Journal of Biomechanics, 2000. 33(4): p. 475-482.

19. Raghavan, M.L., et al., *Wall stress distribution on three-dimensionally reconstructed models of human abdominal aortic aneurysm.* J Vasc Surg, 2000. 31(4): p. 760-9.

20. Reeps, C., et al., *The impact of model assumptions on results of computational mechanics in abdominal aortic aneurysm.* J Vasc Surg, 2010. 51(3): p. 679-88.

21. Thubrikar, M.J., Labrosse, M., Robicsek, F., Al-Soudi, J., Fowler, B., *Mechanical Properties of Abdominal Aortic Aneurysm Wall.* Journal of Medical Engineering and Technology, 2001. 25(4): p. 10.

22. Thubrikar, M.J., J. Al-Soudi, and F. Robicsek, *Wall Stress Studies of Abdominal Aortic Aneurysm in a Clinical Model.* Annals of Vascular Surgery, 2001. 15(3): p. 355-366.

23. Vande Geest, J.P., et al., *A biomechanics-based rupture potential index for abdominal aortic aneurysm risk assessment: demonstrative application.* Ann N Y Acad Sci, 2006. 1085: p. 11-21.

24. He, C.M.R., Margot R, *The composition and mechanical properties of abdominal aortic aneurysms.* Journal of Vascular Surgery, 1994. Volume 20, Number 1: p. 8.

25. Humphrey, J.D. and S. Na, *Elastodynamics and arterial wall stress.* Ann Biomed Eng, 2002. 30(4): p. 509-23.

26. Vorp, D.A., M.L. Raghavan, and M.W. Webster, *Mechanical wall stress in abdominal aortic aneurysm: Influence of diameter and asymmetry.* Journal of Vascular Surgery, 1998. 27(4): p. 632-639.

27. Cowin, S.C.D., Stephen B., *Tissue mechanics* 2007: p. 682.

28. Fung, Y.C., *A First Course in Continuum Mechanics: for physical and biological scientists and enigneers* 1994. 3: p. 311.

29. Lai, M.K., Erhard; Rubin, David, *Introduction to Continuum Mechanics.* 2010: p. 520.

30. Cho, J.-H. and S. Song, *Three-dimensional shape reconstruction from images by shape-from-silhouette technique and iterative triangulation.* Journal of Mechanical Science and Technology, 2003. 17(11): p. 1665-1673.

31. Franco, J.-S.M., Clement; Boyer, Edmond; Raffin, Bruno, *A Distributed Approach for Real Time 3D Modeling.* IEEE 2004: p. 8.

32. Ltd., C.D.S., *3D Software Object Modeler Pro*, 2012 Surrey Technology Centre: Surrey, United Kingdom. p. Shape From Silhouette Reconstruction 2D to 3D reconstruction with Texture Mapping.

33. Sonka, M.H., Vaclav; Boyle, Roger, *Image Processing, Analaysis, and Machine Vision 3rd Edition*. 3rd ed2008, Toronto, Ontario: Thomson Learning. 829.

34. Inc., M., *Matlab* 1994 - 2012: Natick, Massachusetts, U.S.A. p. Programming language for Engineers and Scientists.

35. 2.6, B., *UV Unwrapping of a Mesh.* 2013.

36. Inc., T., *Tecplot 360*, 2010. p. View 3D plots of selected Data in various formats.

37. Systemes, D., *Abaqus* 2010: France. p. Finite Element Analysis.